The Gaussian process distribution of relaxation times: A machine learning tool for the analysis and prediction of electrochemical impedance spectroscopy data

Jiapeng Liu [a], Francesco Ciucci [a, b, *]

[a] The Hong Kong University of Science and Technology, Department of Mechanical and Aerospace Engineering, Clear Water Bay, Sai Kung, Hong Kong Special Administrative Region
[b] The Hong Kong University of Science and Technology, Department of Chemical and Biological Engineering, Clear Water Bay, Sai Kung, Hong Kong Special Administrative Region

ARTICLE INFO

ABSTRACT

Electrochemical impedance spectroscopy (EIS) is one of the most important techniques in electrochemistry. However, analyzing the EIS data is not a simple task. The distribution of relaxation times (DRT) method offers an elegant solution to this considerable challenge. In addition to that, the DRT method can be used to obtain the time characteristics of the electrochemical system under study. Though, deconvolving the DRT from the EIS data is an ill-posed problem, which is particularly sensitive to experimental errors. Several well-known approaches, including ridge regularization, can overcome this issue but they all require the use of *ad hoc* hyperparameters. Furthermore, most methods are not probabilistic and therefore do not provide any uncertainty on the estimated DRT. In this work, by assuming that the DRT is a Gaussian process (GP), it is not only possible to obtain the DRT mean and covariance from the EIS data but also to predict both the DRT and the imaginary part of the impedance at frequencies not previously measured. One important point to note is that, unlike other methods, the parameters that define the GP-DRT model can be selected rationally by maximizing the experimental evidence. The GP-DRT approach is tested using synthetic experiments for analyzing the consistency of the method and "real" experiments to gauge its performance for real data. The GP-DRT model is shown to be able to manage considerable noise, overlapping timescales, truncated data, and inductive features. Considering the GP-DRT framework developed and the results of the simulations, the GP-DRT will likely inspire further studies on using a probabilistic approach to interpret EIS data.

© 2019 Elsevier Ltd. All rights reserved.

1. Introduction

Electrochemical impedance spectroscopy (EIS) is one of the most commonly used characterization techniques in the field of electrochemistry [1–7]. EIS experiments have been used to understand the physicochemical processes taking place in numerous electrochemical systems (ECSs), including fuel cells [8–14], batteries [15–21], solar cells [22,23], and supercapacitors [24]. EIS has also been used in other fields including biology [25–27] and medicine [28,29]. The EIS spectrum is particularly useful because it contains time-dependent information and covers a broad span of timescales, allowing the recovery of many physical properties, such as diffusion coefficients and reaction rate constants [4,30]. During an EIS measurement, the ECS is subjected to a small sinusoidal perturbation in current/bias, and concomitantly the resulting bias/current is recorded [2,5,7]. At a given frequency, the impedance is obtained from the ratio and the dephasing of the bias/current. To obtain the full EIS spectrum, this procedure is repeated over a broad range of frequencies, usually, from mHz to MHz.

Despite the EIS technique being highly effective, interpreting the EIS data can be challenging [31]. To that end, equivalent circuit models (ECMs) [2,5] are often used. However, ECMs have significant limitations. First, they are often chosen in an *ad hoc* fashion and often are just circuit analogs [32]. Second, they are not unique. It is not uncommon to encounter situations where multiple plausible

* Corresponding author. The Hong Kong University of Science and Technology, Department of Mechanical and Aerospace Engineering, Clear Water Bay, Sai Kung, Hong Kong Special Administrative Region.
E-mail address: francesco.ciucci@ust.hk (F. Ciucci).

ECMs can fit the EIS data equally well [33]. Compared to selecting *ad hoc* ECMs, physical models are far more informative of the actual electrochemical processes taking place in the ECS under study [6,22,34−44]. However, physical models are not used as often as ECMs because, as they are system-specific, they require considerable implementation work.

To overcome the challenges mentioned above, the distribution of relaxation times (DRT) has recently attracted significant research attention [45−50]. The idea behind the DRT is to deconvolve the EIS spectrum into a distribution of timescales. This is useful because the time scales can be used to guide the design of ECMs [45] or to identify different physical processes [10,51−56]. The DRT model assumes that the voltage response of an ECS to a step current perturbation decays exponentially with a particular distribution of timescales [46,48]. It can be shown that, if this hypothesis holds, then the impedance can be written as

$$Z^{\text{DRT}}(f) = i2\pi f L_0 + R_\infty + \int_{-\infty}^{\infty} \frac{\gamma(\log \tau)}{1 + i2\pi f \tau} \, d\log \tau \qquad (1)$$

where L_0 is an inductance, R_∞ is a resistance, f is the frequency, and $\gamma(\log\tau)$ is the DRT, which is a function that determines the time-scale distribution [10].

Deconvolving the DRT from the EIS data is not simple because one needs to solve an inverse problem, which is ill-posed [45,49,57]. That is, its solution is particularly sensitive to experimental errors. A variety of numerical frameworks have been developed to resolve ill-posedness and have leveraged methods as diverse as Fourier transform [50], maximum entropy [58], fractional algebraic identification [59], Monte Carlo sampling [60], genetic algorithms [61−63], ridge regression (RR) [47−49,57,64], and elastic-net regularization [65]. One case of particular interest is ridge regression because the DRT deconvolution can be recast as a constrained quadratic programming problem, which solves

Bayesian prior over a functional space [67,68]. First, we assume that the DRT, $\gamma(\log\tau)$, is an unseen (or latent) GP. Second, we note that $\gamma(\log\tau)$ gives the impedance following (1). Using the property that GPs are closed under linear transformations [67,69], the obtained $Z^{\text{DRT}}(f)$ is also a GP. Leveraging the last two properties, we will conduct regression and prediction.

In the following sections, we will first define what GPs are. Using GP regression, we will recover and predict the DRT and the impedance. For all practical purposes, we will use multivariate Gaussian random variables (RVs) to correlate $\gamma(\log\tau)$, $Z^{\text{DRT}}(f)$, and the experimental data. An extremely important point to note is that the hyperparameters do not need to be guessed. Instead, these parameters are obtained by maximizing the experimental evidence, that is, the probability that the experimental result is obtained under the assumptions of the GP model. Furthermore, synthetic experiments as well as "real" experiments show that the GP-DRT model can recover both the DRT and the imaginary part of the impedance well. Lastly, we point out the strengths and weaknesses of the GP-DRT approach and propose future research directions.

2. Theory

2.1. Gaussian processes

2.1.1. Basics

A Gaussian process (GP) can be loosely defined as an infinite collection of RVs, such that every finite subset of these variables follows a multivariate normal distribution [67,68]. Here, we focus on regression and prediction, as is typical of machine learning and assume that the function we wish to learn is a GP. Both GP regression and prediction are Bayesian methods [70]. One should note that such methods are not the same as the frequentist ap-

$$arg\;min_{\boldsymbol{x}\geq 0}\left\{\sum_{n=1}^{N}\left[w_n'\left(Z_{\text{re}}^{\text{exp}}(f_n) - Z_{\text{re}}^{\text{DRT}}(\boldsymbol{x},f_n)\right)^2 + w_n''\left(Z_{\text{im}}^{\text{exp}}(f_n) - Z_{\text{im}}^{\text{DRT}}(\boldsymbol{x},f_n)\right)^2\right]\right\} + \lambda \parallel \boldsymbol{Lx}\parallel^2 \qquad (2)$$

where w_n' and w_n'' are suitable weights, $Z_{\text{re}}^{\text{exp}}$ and $Z_{\text{im}}^{\text{exp}}$ are the real and imaginary part of the experimental impedance, respectively, f_n is the nth frequency, $\boldsymbol{x}$ is an unknown vector that represents the DRT, and $\lambda \boldsymbol{Lx}^2$ is a regularizing term weighted by the hyperparameter λ where $\boldsymbol{L}$ is a suitable differentiation matrix. While the RR can be recast in Bayesian context to recover the DRT and its uncertainty, the choice of the hyperparameter(s) is arbitrary and the only available method is cross-validation [57]. Furthermore, the DRT model has been only used to fit the experimental EIS data and has yet to be used to predict the EIS at frequencies other than the ones measured. This may prove useful in situations where experimental limitations may prevent measurements at certain frequencies (e.g. low frequencies because of time limitations or high frequencies because of instrument limitations) [66].

To overcome the difficulties inherent to selecting hyperparameters and predicting EIS values at unmeasured frequencies, we develop the GP-DRT method. This new method leverages Bayesian statistics and, specifically, Gaussian processes (GPs). Instead of deconvolving the DRT to obtain a simple curve using (2), we interpret the DRT as a GP. It is important to note that GPs in the context of machine learning provides a non-parametric approach for inferring functions from data. Therefore, a GP can be viewed as a

proaches more commonly used in the electrochemical field [2,4,7,32], where one simply fits a model such as an equivalent circuit or a physical model, to the experimental data to obtain an estimate of a parameter. In fact, being Bayesian, the GP-DRT provides the probability distribution function of $\gamma(\log\tau)$ given the experimental observations.

Let us be more formal and consider $g(\mathbf{x})$ as a GP with a mean function $m(\mathbf{x})$ and a covariance (or kernel) function $k(\mathbf{x},\mathbf{x}')$, *i.e.*,

$$g(\mathbf{x}) \sim \mathscr{GP}(m(\mathbf{x}), k(\mathbf{x},\mathbf{x}')) \qquad (3)$$

where $\mathbf{x}$ and $\mathbf{x}'$ both are input points. We remark that $m(\mathbf{x}) = \mathbb{E}[g(\mathbf{x})]$ and that $k(\mathbf{x},\mathbf{x}') = \mathbb{E}[(g(\mathbf{x}) - m(\mathbf{x}))(g(\mathbf{x}') - m(\mathbf{x}'))^\top]$, where $\mathbb{E}[\cdot]$ is the expectation. If we initially assume $m(\mathbf{x}) = 0$ [67,68,70] and take N experimental observations at $\mathbf{x}_1, \mathbf{x}_2, ..., \mathbf{x}_N$, then (3) defines a joint Gaussian distribution $p(g(\mathbf{x}_1), ..., g(\mathbf{x}_N))$ given by

$$p(g(\mathbf{x}_1), ..., g(\mathbf{x}_N)) = \mathscr{N}(0, \mathbf{K}) \qquad (4)$$

where $\mathscr{N}(0, \mathbf{K})$ is the Gaussian or normal probability distribution function with zeros mean and covariance $\mathbf{K}$. $\mathbf{K}$ is defined as $(\mathbf{K})_{ij} = k(\mathbf{x}_i, \mathbf{x}_j)$ with $i,j = 1, 2, \cdots, N$ or as a shorthand $\mathbf{K} = k(\mathbf{X}, \mathbf{X})$ with $\mathbf{X} =$

$(\mathbf{x}_1, \mathbf{x}_2, ..., \mathbf{x}_N)$.

For a given measured dataset $\mathscr{D} = \{(\mathbf{x}_n, y_n), n = 1, 2, ..., N\}$, where the observation y_n is the realization of $g(\mathbf{x}_n)$, we can calculate the posterior, *i.e.*, the probability of g known the data $\mathbf{y} = (y_1, \cdots, y_N)^\top$. More specifically, it can be supposed that the observed dataset $\mathscr{D}$ has noise $\varepsilon \sim \mathscr{N}(0, \sigma_n^2)$, such that $y_n = g(\mathbf{x}_n) + \varepsilon$. Our goal is to predict $g(\mathbf{x}_\star)$, the value of the GP $g(\mathbf{x})$ at an unobserved point $\mathbf{x}_\star$. Following the definition of GP, $\mathbf{y}$ and $g(\mathbf{x}_\star)$ are correlated and have a joint multivariate Gaussian distribution:

$$\begin{pmatrix} \mathbf{y} \\ g(\mathbf{x}_\star) \end{pmatrix} \sim \mathscr{N}\left(0, \begin{pmatrix} \mathbf{K} + \sigma_n^2\mathbf{I} & \mathbf{k}_\star \\ \mathbf{k}_\star^\top & k_{\star\star} \end{pmatrix}\right) \tag{5}$$

where $(\mathbf{k}_\star)_n = k(\mathbf{x}_\star, \mathbf{x}_n)$ or $\mathbf{k}_\star = k(\mathbf{x}_\star, \mathbf{X})$, $k_{\star\star} = k(\mathbf{x}_\star, \mathbf{x}_\star)$, and $\mathbf{I}$ is the identity matrix. As $\mathbf{y}$ is known from the dataset $\mathscr{D}$, the probability distribution function of $g(\mathbf{x}_\star)$ conditioned on $\mathbf{y}$ has the following expression [68], see Appendix A:

$$p(g(\mathbf{x}_\star)|\mathbf{x}_\star, \mathbf{X}, \mathbf{y}) = \mathscr{N}(\mu_{\mathbf{x}_\star}, \Sigma_{\mathbf{x}_\star}) \tag{6}$$

with

$$\mu_{\mathbf{x}_\star} = \mathbf{k}_\star^\top \left(\mathbf{K} + \sigma_n^2\mathbf{I}\right)^{-1} \mathbf{y} \tag{7a}$$

$$\Sigma_{\mathbf{x}_\star} = k_{\star\star} - \mathbf{k}_\star^\top \left(\mathbf{K} + \sigma_n^2\mathbf{I}\right)^{-1} \mathbf{k}_\star \tag{7b}$$

Therefore, this procedure allows the prediction of $g(\mathbf{x}_\star)$ as a normal RV with mean $\mu_{\mathbf{x}_\star}$ and covariance $\Sigma_{\mathbf{x}_\star}$.

2.1.2. Linear transformations of Gaussian processes

One useful property that will be exploited is that GPs are closed under linear transformations [67,69]. This implies that, if a linear functional[1] $\mathscr{L}_\mathbf{x}(\cdot)$ is applied to $g(\mathbf{x})$, then $\mathscr{L}_\mathbf{x}(g(\mathbf{x}))$ is also a GP. In particular, if $g(\mathbf{x})$ is defined as in (3), then

$$\mathscr{L}_\mathbf{x}(g(\mathbf{x})) \sim \mathscr{GP}(0, \mathscr{L}_\mathbf{x}(\mathscr{L}_{\mathbf{x}'}(k(\mathbf{x}, \mathbf{x}')))) \tag{8}$$

and

$$\begin{pmatrix} g(\mathbf{x}) \\ \mathscr{L}_\mathbf{x}(g(\mathbf{x})) \end{pmatrix} \sim \mathscr{GP}\left(0, \begin{pmatrix} k(\mathbf{x}, \mathbf{x}') & \mathscr{L}_{\mathbf{x}'}(k(\mathbf{x}, \mathbf{x}')) \\ \mathscr{L}_\mathbf{x}(k(\mathbf{x}, \mathbf{x}')) & \mathscr{L}_\mathbf{x}(\mathscr{L}_{\mathbf{x}'}(k(\mathbf{x}, \mathbf{x}'))) \end{pmatrix}\right) \tag{9}$$

2.2. The DRT formulation

Here the DRT model given in equation (1) is reformulated so as to exploit the properties illustrated in Section 2.1.2. It should again be noted that the DRT framework rests upon the assumption that we can model the impedance $Z^{\text{DRT}}(f)$ as [46,48]

$$Z^{\text{DRT}}(f) = i2\pi fL_0 + R_\infty + \int_0^\infty \frac{1}{1 + i2\pi f\tau} g(\tau)\, d\tau \tag{10}$$

where $g(\tau)$ is a timescale distribution [10] and $\gamma(\log\tau) = \tau g(\tau)$.[2]

The EIS is usually measured with the frequencies spanning across several orders of magnitude, typically from mHz to MHz. Therefore, it is natural to define the log-frequency $\xi = \log f = -$

log τ, so that (1) can be rewritten as

$$Z_{\text{re}}^{\text{DRT}}(\xi) = R_\infty + \int_{-\infty}^\infty \frac{1}{1 + (2\pi e^{\xi - \widehat{\xi}})^2} \gamma(\widehat{\xi})\, d\widehat{\xi} \tag{11a}$$

$$Z_{\text{im}}^{\text{DRT}}(\xi) = 2\pi fL_0 - \int_{-\infty}^\infty \frac{2\pi e^{\xi - \widehat{\xi}}}{1 + (2\pi e^{\xi - \widehat{\xi}})^2} \gamma(\widehat{\xi})\, d\widehat{\xi} \tag{11b}$$

We indicate $\gamma(\xi)$ as the DRT, which is interchangeably denoted with a notational abuse as $\gamma(\xi)$, $\gamma(\log\tau)$, or $\gamma(\log f)$. We must stress that to keep the notation compact we will use ξ in the ensuing formulas. A similar abuse of notation will be used for $Z^{\text{DRT}}(f)$, which is interchangeably indicated as $Z^{\text{DRT}}(f)$ or $Z^{\text{DRT}}(\xi)$. Without loss of generality [71], we will start our discussion by dropping drop R_∞ and L_0 to rewrite (11) as follows:

$$Z^{\text{DRT}}(\xi) = \mathscr{L}_\xi^{\text{re}}(\gamma(\xi)) + i\mathscr{L}_\xi^{\text{im}}(\gamma(\xi)) \tag{12}$$

where the two functionals $\mathscr{L}_\xi^{\text{re}}(\cdot)$ and $\mathscr{L}_\xi^{\text{im}}(\cdot)$ are defined as

$$\mathscr{L}_\xi^{\text{re}}(\cdot) = \int_{-\infty}^\infty \frac{1}{1 + (2\pi e^{\xi - \widehat{\xi}})^2}(\cdot)\, d\widehat{\xi} \tag{13a}$$

$$\mathscr{L}_\xi^{\text{im}}(\cdot) = -\int_{-\infty}^\infty \frac{2\pi e^{\xi - \widehat{\xi}}}{1 + (2\pi e^{\xi - \widehat{\xi}})^2}(\cdot)\, d\widehat{\xi} \tag{13b}$$

2.3. The GP distribution of relaxation times (GP-DRT)

In this section we recast the DRT model probabilistically using GPs. As already outlined above, we assume that $\gamma(\xi)$ is a latent GP. Formally, as the functionals defined in (13) to $\gamma(\xi)$ are applied, $Z^{\text{DRT}}(\xi)$ is generated via (12). As reported in Section 2.1.2, it follows that $Z^{\text{DRT}}(\xi)$ is also a GP because GPs are closed under linear functionals [67,69], and since $Z^{\text{DRT}}(\xi)$ is derived from $\gamma(\xi)$, the two are correlated. Within this modeling framework, if the impedance data at certain frequencies is given, then one can estimate the latent (or hidden) variable $\gamma(\xi)$ at those frequencies. Since $\gamma(\xi)$ and $Z^{\text{DRT}}(\xi)$ are correlated GPs, one can predict both the DRT and the impedance at any new log-frequency $\xi_\star$. We should note that the GP-DRT approach has several advantages over other DRT regression methods because:

1. We can use the GP-DRT to conduct prediction. In other words, the mean and standard deviation of both impedance and DRT can be computed at frequencies other than those measured experimentally;
2. The hyperparameters of the GP-DRT model can be selected rationally by maximizing the experimental evidence as will be discussed in Section 2.3.4.

For technical reasons, which will be illustrated at the end of this section, we will only use the imaginary part of the impedance to estimate the DRT and to perform predictions. From a practical perspective, we will leverage multivariate Gaussian RVs, especially their conditioning and marginalization. Several useful properties of multivariate Gaussians are given in Appendix A, which the reader is recommended to read.

---

[1] A functional is a function that has as input a function and as output a number.
[2] We note that we use the $\log(\cdot)$ improperly and we should understand that both f and τ are dimensionless variables.

2.3.1. Basics

We start by considering the imaginary part of the impedance and the corresponding functional (13b). First, we assume that $\gamma(\xi)$ is a GP defined as

$$\gamma(\xi) \sim \mathscr{GP}(0, k(\xi, \xi')) \tag{14}$$

Since $Z_{im}^{DRT}(\xi) = \mathscr{L}_{\xi}^{im}(\gamma(\xi))$, see (12), it follows that both $\gamma(\xi)$ and $Z_{im}^{DRT}(\xi)$ are GPs with

$$\begin{pmatrix} \gamma(\xi) \\ Z_{im}^{DRT}(\xi) \end{pmatrix} \sim \mathscr{GP}\left(0, \begin{pmatrix} k(\xi, \xi') & \mathscr{L}_{\xi'}^{im}(k(\xi, \xi')) \\ \mathscr{L}_{\xi}^{im}k(\xi, \xi') & \mathscr{L}_{\xi'}^{im}\left(\mathscr{L}_{\xi}^{im}(k(\xi, \xi'))\right) \end{pmatrix}\right) \tag{15}$$

It is then supposed that the measured impedance is affected by random errors, i.e.,

$$Z_{im}^{exp}(\xi) = Z_{im}^{DRT}(\xi) + \varepsilon \tag{16}$$

where $\varepsilon \sim \mathcal{N}(0, \sigma_n^2)$. All errors are taken to be independent and identically distributed (i.i.d.). Furthermore, we assume to have N observations, which are entered in a random vector $(\mathbf{Z}_{im}^{exp})_n = Z_{im}^{exp}(\xi_n)$ with $\xi_n = \log f_n$ and $n = 1, 2, \ldots N$. The latent variable at the measured frequencies $\boldsymbol{\xi} = (\xi_1, \xi_2, \ldots \xi_N)^{\top}$ is taken to be a random vector such that $(\boldsymbol{\gamma})_n = \gamma(\xi_n)$. Therefore, from (15) and (16), we can write following a line of reasoning similar to the one illustrated in Section 2.1.1 that $(\boldsymbol{\gamma}, \mathbf{Z}_{im}^{exp})^{\top}$ is a multivariate Gaussian RV, i.e.,

$$\begin{pmatrix} \boldsymbol{\gamma} \\ \mathbf{Z}_{im}^{exp} \end{pmatrix} \sim \mathcal{N}\left(0, \begin{pmatrix} \mathbf{K} & \mathscr{L}_{im}\mathbf{K} \\ \mathscr{L}_{im}^{\sharp}\mathbf{K} & \mathscr{L}_{im}^2\mathbf{K} + \sigma_n^2\mathbf{I} \end{pmatrix}\right) \tag{17}$$

where $\mathbf{I}$ is an $N \times N$ identity matrix, and the matrices $\mathbf{K}$, $\mathscr{L}_{im}\mathbf{K}$, $\mathscr{L}_{im}^2\mathbf{K} \in \mathbb{R}^{N \times N}$ are defined as follows ($n, m = 1, \ldots, N$):

$$(\mathbf{K})_{nm} = k(\xi_n, \xi_m) \tag{18a}$$

$$(\mathscr{L}_{im}\mathbf{K})_{nm} = \left|\mathscr{L}_{\xi'}^{im}(k(\xi, \xi'))\right|_{\xi_n, \xi_m} \tag{18b}$$

$$(\mathscr{L}_{im}^{\sharp}\mathbf{K})_{nm} = \left|\mathscr{L}_{\xi}^{im}(k(\xi, \xi'))\right|_{\xi_n, \xi_m} \tag{18c}$$

$$\left(\mathscr{L}_{im}^2\mathbf{K}\right)_{nm} = \left|\mathscr{L}_{\xi'}^{im}\left(\mathscr{L}_{\xi}^{im}(k(\xi, \xi'))\right)\right|_{\xi_n, \xi_m} \tag{18d}$$

From (18) and with an abuse of notation already used in this section, we can define the following matrix-valued functions (see Appendix B for details):

$$\mathbf{K} = \mathbf{K}(\boldsymbol{\xi}, \boldsymbol{\xi}) \tag{19a}$$

$$\mathscr{L}_{im}\mathbf{K} = \mathscr{L}_{im}\mathbf{K}(\boldsymbol{\xi}, \boldsymbol{\xi}) \tag{19b}$$

$$\mathscr{L}_{im}^{\sharp}\mathbf{K} = \mathscr{L}_{im}^{\sharp}\mathbf{K}(\boldsymbol{\xi}, \boldsymbol{\xi}) \tag{19c}$$

$$\mathscr{L}_{im}^2\mathbf{K} = \mathscr{L}_{im}^2\mathbf{K}(\boldsymbol{\xi}, \boldsymbol{\xi}) \tag{19d}$$

where we should note that, as shown in Appendix B, $\mathscr{L}_{im}^{\sharp}\mathbf{K} = \mathscr{L}_{im}\mathbf{K}^{\top}$.

2.3.2. Inversion

Using the GP formulation (15) and (16), we can estimate $\boldsymbol{\gamma}$ given the imaginary part of the experimental impedance. This is done by conditioning $\boldsymbol{\gamma}$ from (17) with respect to $\mathbf{Z}_{im}^{exp}$. In short, we can write that [67].

$$\boldsymbol{\gamma}\big|\mathbf{Z}_{im}^{exp} \sim \mathcal{N}\left(\boldsymbol{\mu}_{\gamma|Z_{im}^{exp}}, \boldsymbol{\Sigma}_{\gamma|Z_{im}^{exp}}\right) \tag{20}$$

where

$$\boldsymbol{\mu}_{\gamma|Z_{im}^{exp}} = \mathscr{L}_{im}\mathbf{K}\left(\mathscr{L}_{im}^2\mathbf{K} + \sigma_n^2\mathbf{I}\right)^{-1}\mathbf{Z}_{im}^{exp} \tag{21a}$$

$$\boldsymbol{\Sigma}_{\gamma|Z_{im}^{exp}} = \mathbf{K} - \mathscr{L}_{im}\mathbf{K}\left(\mathscr{L}_{im}^2\mathbf{K} + \sigma_n^2\mathbf{I}\right)^{-1}\mathscr{L}_{im}\mathbf{K}^{\top} \tag{21b}$$

It should be stressed that the DRT (at the log-frequencies ξ) is a Gaussian RV, whose mean and covariance can be computed analytically using (21). These formulas depend on 1) the kernel, $k(\xi, \xi')$; 2) the noise level, σ_n; and 3) the experimental data, $\mathbf{Z}_{im}^{exp}$ (at the log-frequencies ξ). In Section 2.3.4 we will show one method to select the hyperparameters, the parameters of the kernel and the σ_n.

2.3.3. Prediction

The GP-DRT can also be used to predict the impedance at a log-frequency $\xi_{\star}$, which was not measured before. We can perform such a prediction by noting that, since both (15) and (16) hold, the joint distribution of latent $\boldsymbol{\gamma}$, target ($\mathbf{Z}_{im}^{exp}$), and predicted $(\gamma(\xi_{\star}), Z_{im}^{DRT}(\xi_{\star}))^{\top}$ RVs follows a multivariate Gaussian distribution. Therefore, we can write

$$\begin{pmatrix} \boldsymbol{\gamma} \\ \mathbf{Z}_{im}^{exp} \\ \gamma(\xi_{\star}) \\ Z_{im}^{DRT}(\xi_{\star}) \end{pmatrix} \sim \mathcal{N}(0, \boldsymbol{\Sigma}) \tag{22}$$

where

$$\boldsymbol{\Sigma} = \begin{pmatrix} \mathbf{K} & \mathscr{L}_{im}\mathbf{K} & \mathbf{K}(\boldsymbol{\xi}, \xi_{\star}) & \mathscr{L}_{im}\mathbf{K}(\boldsymbol{\xi}, \xi_{\star}) \\ \mathscr{L}_{im}^{\sharp}\mathbf{K} & \mathscr{L}_{im}^2\mathbf{K} + \sigma_n^2\mathbf{I} & \mathscr{L}_{im}^{\sharp}\mathbf{K}(\boldsymbol{\xi}, \xi_{\star}) & \mathscr{L}_{im}^2\mathbf{K}(\boldsymbol{\xi}, \xi_{\star}) \\ \mathbf{K}(\xi_{\star}, \boldsymbol{\xi}) & \mathscr{L}_{im}\mathbf{K}(\xi_{\star}, \boldsymbol{\xi}) & k(\xi_{\star}, \xi_{\star}) & \mathscr{L}_{im}k(\xi_{\star}, \xi_{\star}) \\ \mathscr{L}_{im}^{\sharp}\mathbf{K}(\xi_{\star}, \boldsymbol{\xi}) & \mathscr{L}_{im}^2\mathbf{K}(\xi_{\star}, \boldsymbol{\xi}) & \mathscr{L}_{im}^{\sharp}k(\xi_{\star}, \xi_{\star}) & \mathscr{L}_{im}^2k(\xi_{\star}, \xi_{\star}) \end{pmatrix} \tag{23}$$

It follows directly from (22) that

$$\begin{pmatrix} \mathbf{Z}_{im}^{exp} \\ Z_{im}^{DRT}(\xi_{\star}) \end{pmatrix} \sim \mathcal{N}\left(0, \begin{pmatrix} \mathscr{L}_{im}^2\mathbf{K} + \sigma_n^2\mathbf{I} & \mathscr{L}_{im}^2\mathbf{K}(\boldsymbol{\xi}, \xi_{\star}) \\ \mathscr{L}_{im}^2\mathbf{K}(\boldsymbol{\xi}, \xi_{\star})^{\top} & \mathscr{L}_{im}^2k(\xi_{\star}, \xi_{\star}) \end{pmatrix}\right) \tag{24}$$

Therefore $Z_{im}^{DRT}(\xi_{\star})$, i.e., the imaginary part of the impedance predicted at $\xi_{\star}$, is an RV that can be obtained from the imaginary part of the experimental EIS data, $\mathbf{Z}_{im}^{exp}$, using the conditional distribution [68,72].

$$Z_{im}^{DRT}(\xi_{\star})\big|\mathbf{Z}_{im}^{exp} \sim \mathcal{N}\left(\mu_{Z_{im\star}^{DRT}}, \Sigma_{Z_{im\star}^{DRT}}\right) \tag{25}$$

where

$$
\begin{pmatrix} \gamma(\xi) \\ Z_{\mathrm{re}}^{\mathrm{DRT}}(\xi) \\ Z_{\mathrm{im}}^{\mathrm{DRT}}(\xi) \end{pmatrix} \sim \mathscr{GP}\left(0, \begin{pmatrix} k(\xi,\xi') & \mathscr{L}_{\xi'}^{\mathrm{re}}(k(\xi,\xi')) & \mathscr{L}_{\xi'}^{\mathrm{im}}(k(\xi,\xi')) \\ \mathscr{L}_{\xi}^{\mathrm{re}}(k(\xi,\xi')) & \mathscr{L}_{\xi'}^{\mathrm{re}}\left(\mathscr{L}_{\xi}^{\mathrm{re}}(k(\xi,\xi'))\right) & \mathscr{L}_{\xi'}^{\mathrm{im}}\left(\mathscr{L}_{\xi}^{\mathrm{re}}(k(\xi,\xi'))\right) \\ \mathscr{L}_{\xi}^{\mathrm{im}}(k(\xi,\xi')) & \mathscr{L}_{\xi'}^{\mathrm{re}}\left(\mathscr{L}_{\xi}^{\mathrm{im}}(k(\xi,\xi'))\right) & \mathscr{L}_{\xi'}^{\mathrm{im}}\left(\mathscr{L}_{\xi}^{\mathrm{im}}(k(\xi,\xi'))\right) \end{pmatrix} \right)
$$
(34)

$$
\mu_{Z_{\mathrm{im}\star}^{\mathrm{DRT}}} = \mathscr{L}_{\mathrm{im}}^2 \mathbf{K}(\xi,\xi_\star)^\top \left(\mathscr{L}_{\mathrm{im}}^2 \mathbf{K} + \sigma_n^2 \mathbf{I} \right)^{-1} \mathbf{Z}_{\mathrm{im}}^{\mathrm{exp}}
$$
(26a)

$$
\Sigma_{Z_{\mathrm{im}\star}^{\mathrm{DRT}}} = \mathscr{L}_{\mathrm{im}}^2 k(\xi_\star,\xi_\star)
$$
$$
- \mathscr{L}_{\mathrm{im}}^2 \mathbf{K}(\xi,\xi_\star)^\top \left(\mathscr{L}_{\mathrm{im}}^2 \mathbf{K} + \sigma_n^2 \mathbf{I} \right)^{-1} \mathscr{L}_{\mathrm{im}}^2 \mathbf{K}(\xi,\xi_\star)
$$
(26b)

It also follows from (22) and (23) that

$$
\begin{pmatrix} \mathbf{Z}_{\mathrm{im}}^{\mathrm{exp}} \\ \gamma(\xi_\star) \end{pmatrix} \sim \mathscr{N}\left(0, \begin{pmatrix} \mathscr{L}_{\mathrm{im}}^2 \mathbf{K} + \sigma_n^2 \mathbf{I} & \mathscr{L}_{\mathrm{im}} \mathbf{K}(\xi_\star,\xi)^\top \\ \mathscr{L}_{\mathrm{im}} \mathbf{K}(\xi_\star,\xi) & k(\xi_\star,\xi_\star) \end{pmatrix} \right)
$$
(27)

where we note $\mathscr{L}_{\mathrm{im}}^\sharp \mathbf{K}(\xi,\xi_\star) = \mathscr{L}_{\mathrm{im}} \mathbf{K}(\xi_\star,\xi)^\top$. Again, by conditioning we can write

$$
\gamma(\xi_\star) \big| \mathbf{Z}_{\mathrm{im}}^{\mathrm{exp}} \sim \mathscr{N}(\mu_{\gamma_\star}, \Sigma_{\gamma_\star})
$$
(28)

with

$$
\mu_{\gamma_\star} = \mathscr{L}_{\mathrm{im}} \mathbf{K}(\xi_\star,\xi) \left(\mathscr{L}_{\mathrm{im}}^2 \mathbf{K} + \sigma_n^2 \mathbf{I} \right)^{-1} \mathbf{Z}_{\mathrm{im}}^{\mathrm{exp}}
$$
(29a)

$$
\Sigma_{\gamma_\star} = k(\xi_\star,\xi_\star) - \mathscr{L}_{\mathrm{im}} \mathbf{K}(\xi_\star,\xi) \left(\mathscr{L}_{\mathrm{im}}^2 \mathbf{K} + \sigma_n^2 \mathbf{I} \right)^{-1} \mathscr{L}_{\mathrm{im}} \mathbf{K}(\xi_\star,\xi)^\top
$$
(29b)

This derivation implies that the $\gamma(\xi_\star)$ can also be predicted given the experimental data $\mathbf{Z}_{\mathrm{im}}^{\mathrm{exp}}$.

2.3.4. Selecting the hyperparameters

As already illustrated in Section 2.3.2, the matrix formulas given above for means and covariances depend on the experimental data and the hyperpameters of the model. While during the data analysis phase there is little control over the experimental data, all hyperparameters can be chosen, including the kernel $k(\xi,\xi')$ and the (unknown) noise level σ_n. Hereon, we constrain the kernel to be a squared exponential, *i.e.*,

$$
k(\xi,\xi') = \sigma_f^2 \exp\left(-\frac{1}{2\ell^2}(\xi - \xi')^2 \right)
$$
(30)

and we will modify its two parameters, σ_f and ℓ. Therefore, the vector of hyperparameters of the GP-DRT is assumed to be $\boldsymbol{\theta} = (\sigma_n, \sigma_f, \ell)^\top$.

A $\boldsymbol{\theta}$ can be selected by maximizing the marginal likelihood, the probability, $p(\mathbf{Z}_{\mathrm{im}}^{\mathrm{exp}}|\xi,\boldsymbol{\theta})$[3] of measuring the data, $\mathbf{Z}_{\mathrm{im}}^{\mathrm{exp}}$. The

maximizing $\boldsymbol{\theta}$ is the one that would have most likely resulted in the measured experimental data. We note that $\mathbf{Z}_{\mathrm{im}}^{\mathrm{exp}}\big|\boldsymbol{\theta} \sim \mathscr{N}(0, \mathscr{L}_{\mathrm{im}}^2 \mathbf{K} + \sigma_n^2 \mathbf{I})$. Therefore, we obtain the following marginal log-likelihood (MLL) [72]:

$$
\log p\left(\mathbf{Z}_{\mathrm{im}}^{\mathrm{exp}}\big|\xi,\boldsymbol{\theta}\right) = -\frac{1}{2}\mathbf{Z}_{\mathrm{im}}^{\mathrm{exp}\top} \left(\mathscr{L}_{\mathrm{im}}^2 \mathbf{K} + \sigma_n^2 \mathbf{I} \right)^{-1} \mathbf{Z}_{\mathrm{im}}^{\mathrm{exp}}
$$
$$
+ -\frac{1}{2}\log\left|\mathscr{L}_{\mathrm{im}}^2 \mathbf{K} + \sigma_n^2 \mathbf{I}\right| - \frac{N}{2}\log 2\pi
$$
(31)

We will call $L(\boldsymbol{\theta})$ the negative (and shifted) MLL (NMLL):

$$
L(\boldsymbol{\theta}) = -\log p\left(\mathbf{Z}_{\mathrm{im}}^{\mathrm{exp}}|\xi,\boldsymbol{\theta}\right) - \frac{N}{2}\log 2\pi
$$
(32)

It follows that the experimental evidence is maximized for

$$
\boldsymbol{\theta} = \arg\min_{\boldsymbol{\theta}'} L(\boldsymbol{\theta}')
$$
(33)

We also note that, in order to minimize $L(\boldsymbol{\theta})$, one may use a gradient-based method which requires the computation of $\nabla L(\boldsymbol{\theta})$. This can be done analytically as shown in Appendix C.

2.3.5. Comment

It would haven been tempting to combine the real and imaginary parts of the impedance formally. We note that if the DRT model (12) and (14) hold, then the following also holds:

However, we must remark that, as shown in Appendix B,

$$
\mathscr{L}_{\xi'}^{\mathrm{re}}\left(\mathscr{L}_{\xi}^{\mathrm{re}}(k(\xi,\xi'))\right) = \infty
$$
(35)

The covariance being infinite renders impractical the use of the real part of the impedance. While we will not attempt to use such a portion of the data, we will discuss in Section 4 how this issue could be overcome.

2.4. The GP-DRT with inductance

In this section we are going to relax the hypothesis that $L_0 = 0$ used in (12), and, instead, set that

$$
\begin{pmatrix} \gamma(\xi) \\ Z_{\mathrm{im}}^{\mathrm{DRT}}(\xi) \end{pmatrix} \sim L_0 \begin{pmatrix} 0 \\ 2\pi e^\xi \end{pmatrix}
$$
$$
+ \mathscr{GP}\left(0, \begin{pmatrix} k(\xi,\xi') & \mathscr{L}_{\xi'}^{\mathrm{im}}(k(\xi,\xi')) \\ \mathscr{L}_{\xi}^{\mathrm{im}}(k(\xi,\xi')) & \mathscr{L}_{\xi'}^{\mathrm{im}}\left(\mathscr{L}_{\xi}^{\mathrm{im}}(k(\xi,\xi'))\right) \end{pmatrix} \right)
$$
(36)

where L_0 is a normally distributed RV, *i.e.*, $L_0 \sim \mathscr{N}(0, \sigma_L^2)$, independent with respect to the right hand side's GP, which is identical to the GP defined in (15). If we integrate out the L_0 in (36), we can write [70,71].

---

[3] We emphasize pedantically the conditioning with respect to ξ and $\boldsymbol{\theta}$ as both parameters influence the evidence.

$$\begin{pmatrix} \gamma(\xi) \\ Z_{\mathrm{im}}^{\mathrm{DRT}}(\xi) \end{pmatrix} \sim \mathscr{GP}\left(0, \begin{pmatrix} k(\xi, \xi') & \mathscr{L}_{\xi'}^{\mathrm{im}}(k(\xi, \xi')) \\ \mathscr{L}_{\xi}^{\mathrm{im}}(k(\xi, \xi')) & \mathscr{L}_{\xi'}^{\mathrm{im}}\left(\mathscr{L}_{\xi}^{\mathrm{im}}(k(\xi, \xi'))\right) + \sigma_L^2 h(\xi) h(\xi') \end{pmatrix}\right) \tag{37}$$

where $h(\xi) = 2\pi e^{\xi}$. Therefore, using the same procedure used for (17), we obtain

$$\begin{pmatrix} \gamma \\ \mathbf{Z}_{\mathrm{im}}^{\mathrm{exp}} \end{pmatrix} \sim \mathscr{N}\left(0, \begin{pmatrix} \mathbf{K} & \mathscr{L}_{\mathrm{im}}\mathbf{K} \\ \mathscr{L}_{\mathrm{im}}^{\sharp}\mathbf{K} & \mathscr{L}_{\mathrm{im}}^2\mathbf{K} + \sigma_n^2\mathbf{I} + \sigma_L^2\mathbf{h}\,\mathbf{h}^{\top} \end{pmatrix}\right) \tag{38}$$

where $\mathbf{h} = (h(\xi_1), h(\xi_2), \ldots, h(\xi_N))^{\top}$. With an analogous procedure as the one used to derive (22) and (23), we can also write

$$\begin{pmatrix} \gamma \\ \mathbf{Z}_{\mathrm{im}}^{\mathrm{exp}} \\ \gamma(\xi_{\star}) \\ Z_{\mathrm{im}}^{\mathrm{DRT}}(\xi_{\star}) \end{pmatrix} \sim \mathscr{N}(0, \mathbf{\Sigma}) \tag{39}$$

where

$$\mathbf{\Sigma} = \begin{pmatrix} \mathbf{K} & \mathscr{L}_{\mathrm{im}}\mathbf{K} & \mathbf{K}(\xi, \xi_{\star}) & \mathscr{L}_{\mathrm{im}}\mathbf{K}(\xi, \xi_{\star}) \\ \mathscr{L}_{\mathrm{im}}^{\sharp}\mathbf{K} & \mathscr{L}_{\mathrm{im}}^2\mathbf{K} + \sigma_n^2\mathbf{I} + \sigma_L^2\mathbf{h}\,\mathbf{h}^{\top} & \mathscr{L}_{\mathrm{im}}^{\sharp}\mathbf{K}(\xi, \xi_{\star}) & \mathscr{L}_{\mathrm{im}}^2\mathbf{K}(\xi, \xi_{\star}) + \sigma_L^2 h(\xi_{\star})\mathbf{h} \\ \mathbf{K}(\xi_{\star}, \xi) & \mathscr{L}_{\mathrm{im}}\mathbf{K}(\xi_{\star}, \xi) & k(\xi_{\star}, \xi_{\star}) & \mathscr{L}_{\mathrm{im}}k(\xi_{\star}, \xi_{\star}) \\ \mathscr{L}_{\mathrm{im}}^{\sharp}\mathbf{K}(\xi_{\star}, \xi) & \mathscr{L}_{\mathrm{im}}^2\mathbf{K}(\xi_{\star}, \xi) + \sigma_L^2 h(\xi_{\star})\mathbf{h}^{\top} & \mathscr{L}_{\mathrm{im}}^{\sharp}k(\xi_{\star}, \xi_{\star}) & \mathscr{L}_{\mathrm{im}}^2 k(\xi_{\star}, \xi_{\star}) + \sigma_L^2 h(\xi_{\star})^2 \end{pmatrix} \tag{40}$$

It follows directly from (39) and (40) that

$$\begin{pmatrix} \mathbf{Z}_{\mathrm{im}}^{\mathrm{exp}} \\ Z_{\mathrm{im}}^{\mathrm{DRT}}(\xi_{\star}) \end{pmatrix} \sim \mathscr{N}\left(0, \begin{pmatrix} \mathscr{L}_{\mathrm{im}}^2\mathbf{K} + \sigma_n^2\mathbf{I} + \sigma_L^2\mathbf{h}\,\mathbf{h}^{\top} & \mathscr{L}_{\mathrm{im}}^2\mathbf{K}(\xi, \xi_{\star}) + \sigma_L^2 h(\xi_{\star})\mathbf{h} \\ \mathscr{L}_{\mathrm{im}}^2\mathbf{K}(\xi, \xi_{\star})^{\top} + \sigma_L^2 h(\xi_{\star})\mathbf{h}^{\top} & \mathscr{L}_{\mathrm{im}}^2 k(\xi_{\star}, \xi_{\star}) + \sigma_L^2 h(\xi_{\star})^2 \end{pmatrix}\right) \tag{41}$$

By conditioning $Z_{\mathrm{im}}^{\mathrm{DRT}}(\xi_{\star})$ to the data, we can write [71].

$$Z_{\mathrm{im}}^{\mathrm{DRT}}(\xi_{\star}) \big| \mathbf{Z}_{\mathrm{im}}^{\mathrm{exp}} \sim \mathscr{N}\left(\mu_{Z_{\mathrm{im}\star}^{\mathrm{DRT}}}^L, \Sigma_{Z_{\mathrm{im}\star}^{\mathrm{DRT}}}^L\right) \tag{42}$$

where

$$\mu_{Z_{\mathrm{im}\star}^{\mathrm{DRT}}}^L = h(\xi_{\star})\bar{L}_0 + \mathscr{L}_{\mathrm{im}}^2\mathbf{K}(\xi, \xi_{\star})^{\top}\left(\mathscr{L}_{\mathrm{im}}^2\mathbf{K} + \sigma_n^2\mathbf{I}\right)^{-1}\left(\mathbf{Z}_{\mathrm{im}}^{\mathrm{exp}} - \mathbf{h}^{\top}\bar{L}_0\right) \tag{43a}$$

$$\Sigma_{Z_{\mathrm{im}\star}^{\mathrm{DRT}}}^L = \Sigma_{Z_{\mathrm{im}\star}^{\mathrm{DRT}}} + \frac{R^2}{\sigma_L^{-2} + \mathbf{h}^{\top}\left(\mathscr{L}_{\mathrm{im}}^2\mathbf{K} + \sigma_n^2\mathbf{I}\right)^{-1}\mathbf{h}} \tag{43b}$$

with

$$\bar{L}_0 = \frac{\mathbf{h}^{\top}\left(\mathscr{L}_{\mathrm{im}}^2\mathbf{K} + \sigma_n^2\mathbf{I}\right)^{-1}\mathbf{Z}_{\mathrm{im}}^{\mathrm{exp}}}{\sigma_L^{-2} + \mathbf{h}^{\top}\left(\mathscr{L}_{\mathrm{im}}^2\mathbf{K} + \sigma_n^2\mathbf{I}\right)^{-1}\mathbf{h}} \tag{44a}$$

$$R = h(\xi_{\star}) - \mathbf{h}\left(\mathscr{L}_{\mathrm{im}}^2\mathbf{K} + \sigma_n^2\mathbf{I}\right)^{-1}\mathscr{L}_{\mathrm{im}}\mathbf{K}(\xi_{\star}, \xi)^{\top} \tag{44b}$$

Similarly, we obtain that

$$\begin{pmatrix} \mathbf{Z}_{\mathrm{im}}^{\mathrm{exp}} \\ \gamma(\xi_{\star}) \end{pmatrix} \sim \mathscr{N}\left(0, \begin{pmatrix} \mathscr{L}_{\mathrm{im}}^2\mathbf{K} + \sigma_n^2\mathbf{I} + \sigma_L^2\mathbf{h}\,\mathbf{h}^{\top} & \mathscr{L}_{\mathrm{im}}\mathbf{K}(\xi_{\star}, \xi)^{\top} \\ \mathscr{L}_{\mathrm{im}}\mathbf{K}(\xi_{\star}, \xi) & k(\xi_{\star}, \xi_{\star}) \end{pmatrix}\right) \tag{45}$$

therefore

$$\gamma(\xi_{\star}) \big| \mathbf{Z}_{\mathrm{im}}^{\mathrm{exp}} \sim \mathscr{N}(\mu_{\gamma_{\star}}, \Sigma_{\gamma_{\star}}) \tag{46}$$

with

$$\mu_{\gamma_{\star}} = \mathscr{L}_{\mathrm{im}}\mathbf{K}(\xi_{\star}, \xi)\left(\mathscr{L}_{\mathrm{im}}^2\mathbf{K} + \sigma_n^2\mathbf{I} + \sigma_L^2\mathbf{h}\,\mathbf{h}^{\top}\right)^{-1}\mathbf{Z}_{\mathrm{im}}^{\mathrm{exp}} \tag{47a}$$

$$\begin{aligned} \Sigma_{\gamma_{\star}} = &\, k(\xi_{\star}, \xi_{\star}) \\ &- \mathscr{L}_{\mathrm{im}}\mathbf{K}(\xi_{\star}, \xi)\left(\mathscr{L}_{\mathrm{im}}^2\mathbf{K} + \sigma_n^2\mathbf{I} + \sigma_L^2\mathbf{h}\,\mathbf{h}^{\top}\right)^{-1}\mathscr{L}_{\mathrm{im}}\mathbf{K}(\xi_{\star}, \xi)^{\top} \end{aligned} \tag{47b}$$

As shown previously in Section 2.3.4, we can also derive the marginal log-likelihood (MLL), which, under the assumptions of this subsection, is given by
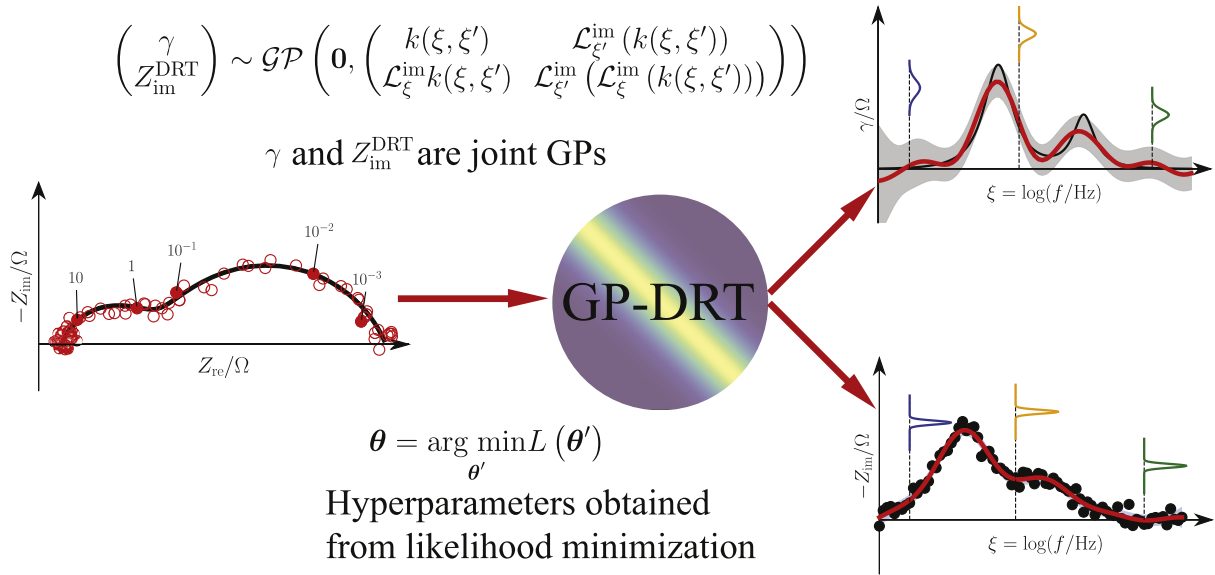
$$\begin{pmatrix} \gamma \\ Z_{\mathrm{im}}^{\mathrm{DRT}} \end{pmatrix} \sim \mathcal{GP}\left(\mathbf{0}, \begin{pmatrix} k(\xi,\xi') & \mathcal{L}_{\xi'}^{\mathrm{im}}\left(k(\xi,\xi')\right) \\ \mathcal{L}_{\xi}^{\mathrm{im}}k(\xi,\xi') & \mathcal{L}_{\xi'}^{\mathrm{im}}\left(\mathcal{L}_{\xi}^{\mathrm{im}}\left(k(\xi,\xi')\right)\right) \end{pmatrix}\right)$$

γ and $Z_{\mathrm{im}}^{\mathrm{DRT}}$ are joint GPs

$$\boldsymbol{\theta} = \arg\min_{\boldsymbol{\theta}'} L\left(\boldsymbol{\theta}'\right)$$

Hyperparameters obtained
from likelihood minimization

Fig. 1. Schematic illustration of the GP-DRT framework.

$$\log p\left(\mathbf{Z}_{\mathrm{im}}^{\mathrm{exp}}\middle|\xi,\boldsymbol{\theta}\right) = -\frac{1}{2}\mathbf{Z}_{\mathrm{im}}^{\mathrm{exp}\top}\left(\mathscr{L}_{\mathrm{im}}^{2}\mathbf{K} + \sigma_n^2\mathbf{I} + \sigma_L^2\mathbf{h}\mathbf{h}^\top\right)^{-1}\mathbf{Z}_{\mathrm{im}}^{\mathrm{exp}}$$
$$+ -\frac{1}{2}\log\left|\mathscr{L}_{\mathrm{im}}^{2}\mathbf{K} + \sigma_n^2\mathbf{I} + \sigma_L^2\mathbf{h}\mathbf{h}^\top\right| - \frac{N}{2}\log 2\pi$$

(48)

Table 1
Parameters used for the exact impedance model.

Parameter	Numerical Value
R_∞	10 Ω
R_{ct}	50 Ω
τ_0	1 s
τ_1	0.1 s
τ_2	10 s
ϕ	0.8
L_0	5.0×10^{-4} F

3. Results

The GP-DRT model, schematically shown in Fig. 1, will be tested using both synthetic and real experimental data. First, the synthetic experiments are analyzed to test the consistency of the methodology. Specifically, since the exact impedance and DRT are both known a priori, it will be verified that the GP-DRT can recover both quantities. In doing that, the influence of the hyperparameters on both inversion and prediction are illustrated. Furthermore, it will be shown that these hyperparameters can be chosen optimally. It is also demonstrated that the GP-DRT is robust to noise, missing data, and overlapping features in the timescale distribution. As a second step, the GP-DRT framework will be applied to actual experiments in order to gauge its capability to handle real data. In particular, the GP-DRT model is benchmarked against the previously developed Bayesian DRT methodology [49,57,73].

3.1. Synthetic experiments

In this subsection the GP-DRT model is tested against synthetic experiments to ensure its consistency. The influence of the hyperparameters is also illustrated. Further, the GP-DRT is shown to be able to consistently handle severe noise, spectral truncation, bimodal timescale distributions, and inductive features. Before starting a systematic analysis of the synthetic and real EIS data, we recall that we will use interchangeably $\gamma(\log\tau)$, $\gamma(\log f)$, or $\gamma(\xi)$ and that a similar notational abuse also applies to $Z_{\mathrm{im}}^{\mathrm{DRT}}(f)$ and $Z_{\mathrm{im}}^{\mathrm{DRT}}(\xi)$.

3.1.1. Exact impedance

The analysis of the synthetic data is primarily based on the impedance of a ZARC element consisting of a resistance placed in parallel to a constant phase element (CPE) [74]. The $Z^{\mathrm{exact}}(f)$ is therefore given by

$$Z^{\mathrm{exact}}(f) = R_\infty + \frac{1}{\frac{1}{R_{\mathrm{ct}}} + C(i2\pi f)^\phi}$$

(49)

where $C = \frac{\tau_0^\phi}{R_{\mathrm{ct}}}$ and the specific parameters used are shown in Table 1. As is well known, the DRT of (49) is given by Ref. [75].

$$\gamma(\log\tau) = \frac{R_{\mathrm{ct}}}{2\pi} \frac{\sin((1-\phi)\pi)}{\cosh(\phi\log(\tau/\tau_0)) - \cos(\pi(1-\phi))}$$

(50)

In Fig. 2, we report the Nyquist representation of the impedance, panel (a), and the DRT, panel (b). This shows both the exact impedance given by (49) and its noise-corrupted counterpart $Z^{\mathrm{exp}}(f)$ given by (16), where we set $\sigma_n = \sigma_n^{\mathrm{exp}} = 0.1 \ \Omega^{1/2}$.[4] We recall once more that the current version of the GP-DRT model does not use the real part of the impedance data.

3.1.2. Qualitative considerations

Starting from the synthetic data, we illustrate the influence of the hyperparameters on the recovery of the latent DRT, $\gamma(\xi)$, and the imaginary part of the impedance $Z_{\mathrm{im}}^{\mathrm{DRT}}(f)$.

First we set $\sigma_f = 1$ and $\sigma_n = \sigma_n^{\mathrm{exp}}$. As shown in Fig. 3, changing

---

[4] We note that this expression is an abuse of notation because σ_n is *de facto* an hyperparameter, while σ_n^{exp} is the amount of noise given to the synthetic experiment.
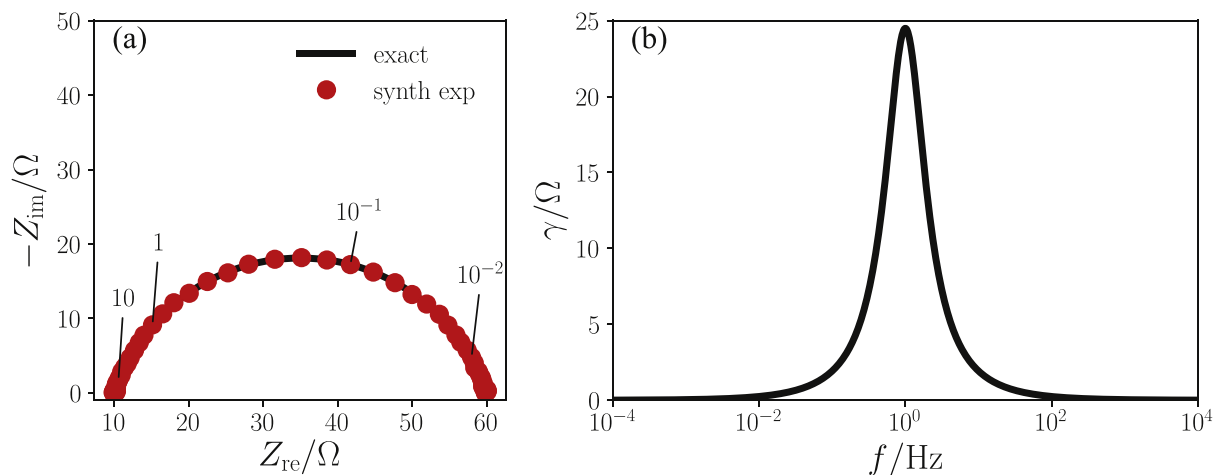
Fig. 2. (a) Nyquist plot of the exact ZARC impedance, Z, (solid line) and the synthetic experimental data (red dots) ($\sigma_n^{exp} = 0.1\ \Omega^{1/2}$), and (b) the corresponding exact DRT, γ. Note $\xi = \log f$. (For interpretation of the references to colour in this figure legend, the reader is referred to the Web version of this article.)

the length scale ℓ of the kernel has a dramatic influence on the recovered $\gamma(\xi)$ and $Z_{im}^{DRT}(f)$. In the left-hand panels, we report the exact and the inverted DRT given by equations (50) and (20), respectively. The right-hand panels depict instead the imaginary part of the impedance including its exact value, the synthetic experiment, and the recovered value from (24). As the standard deviations are small, only the mean (red line) is visible.

A small ℓ (here we have $\ell = 10^{-2}$), see panels (a) and (b) of Fig. 3, is indicative of only short range log-frequency correlations (30). This choice results in: 1) a rather large variance as indicated by the shaded area around the mean (red line), see Fig. 3 (a); and 2) a significant discrepancy compared to the experimental impedance, see Fig. 3 (b). The DRT peak is lower than the exact one and does not result in significant oscillations at either low or high frequencies. Raising the value of ℓ to 1 gives a closer matching of the peak height in the DRT, see Fig. 3 (c), and an improved recovery of the imaginary part of the impedance as shown in Fig. 3 (d). It also leads to a greater confidence in the recovered DRT as shown by the far smaller shaded area. However, oscillations are stronger at both low and high log-frequencies. This is in contrast with the $\ell = 10^{-2}$ case, where the shorter-range log-frequency correlations hamper the oscillations. Increasing ℓ by an order of magnitude to 10 has a deleterious impact on both the inverted $\gamma(\xi)$, see Fig. 3 (e), and the recovered impedance $Z_{im}^{DRT}(f)$, see Fig. 3 (f). Under these circumstances, the correlations are so broad that both $\gamma(\xi)$ and $Z_{im}^{DRT}(f)$ effectively flatten out.

To better understand the results presented above, let us directly inspect $\mathbf{K}$ and $\mathscr{L}^2\mathbf{K}$, two of the important matrices used in Section 2.3 and given by (18). The parameter ℓ strongly influences both matrices, as shown in Fig. 4. Choosing a relative short cross-correlation scale ($\ell = 10^{-2}$) results in a diagonally dominated $\mathbf{K}$ matrix, see Fig. 4 (a). The fact that $\mathbf{K}$ is mostly diagonal implies that the value $\gamma(\xi)$ at a certain log-frequency ξ is only influenced by a small number of ξ values directly adjacent to it. Applying the functional (13b) twice gives the $\mathscr{L}^2\mathbf{K}$ as illustrated in (18d). Since the integral is convolutive in nature, the number of non-zero entries in the $\mathscr{L}^2\mathbf{K}$ matrix increases relative to those in $\mathbf{K}$, see Fig. 4 (b). This means that $\mathscr{L}^2\mathbf{K}$ implies far broader correlations than $\mathbf{K}$. In other words, while the DRT may not strongly cross-correlated across the log-frequencies for low enough ℓ, the values of the $Z_{im}^{DRT}(f)$ depend on each other across a far broader spectrum. As

shown in Fig. 4 (c) and (d), increasing ℓ to 1 broadens $\mathscr{L}^2\mathbf{K}$ more strongly compared to the $\ell = 10^{-2}$ case. This is also in agreement with intuition and the results that relate to Fig. 3 (c) and (d). As already illustrated when discussing Fig. 3 (c) and (d), increasing ℓ to 1 has a positive impact on the recovery of $Z_{im}^{DRT}(f)$ but yields stronger oscillations in the $\gamma(\xi)$.

3.1.3. Hyperparameter optimization

We show now how the hyperparameters can be optimized based on the experimental data. We will not only change ℓ parametrically as done in Section 3.1.2 but we will also set all values in the vector $\boldsymbol{\theta} = (\sigma_n, \sigma_f, \ell)$. For illustration purposes, we start by varying only two elements of $\boldsymbol{\theta}$ ($\sigma_f = 1$) and show the $L(\boldsymbol{\theta})$ given by (32) as a function of σ_n and ℓ. We recall that, as explained in Section 2.3.4, $L(\boldsymbol{\theta})$ is closely linked to the maximum likelihood and minimizing this function corresponds to maximizing the experimental evidence. At the minimum the model output, $Z_{im}^{DRT}(f)$, is closest to the synthetic experiment, $Z_{im}^{exp}(f)$. In other words, the minimized hyperparameters are the ones that best comply with the data, which is illustrated this in Fig. 5. From Fig. 5 (a), we observe that the minimum in the (ℓ, σ_n) plane is obtained for $\sigma_n \approx \sigma_n^{exp}$, consistently with the value of the added noise. The ℓ is approximately equal to 1, the value used for some of the results presented in Section 3.1.2 above. We then set (ℓ, σ_n) to be equal to its value at the star symbol in Fig. 5 (a) and seek a σ_f which can further minimize the $L(\boldsymbol{\theta})$. Fig. 5 (b) shows that a rather sharp minimum can be located at $\sigma_f \approx 5$ further improving the adherence of the model with the synthetic experiment. However, it must be noted that this is not the true minimum of $L(\boldsymbol{\theta})$. The latter can be instead obtained by minimizing all entries of the vector $\boldsymbol{\theta}$ simultaneously. The obtained value $\boldsymbol{\theta}$ shown in Table 2 (case 1) gives the $\gamma(\xi)$ and $Z_{im}^{DRT}(f)$ shown in Fig. 5 (c) and (d), respectively. Unsurprisingly, this value improves (at least visually) the recovery of the imaginary part of the impedance $Z_{im}^{DRT}(f)$, see Fig. 5 (d). Minimizing $L(\boldsymbol{\theta})$ yields the latent DRT, $\gamma(\xi)$, shown in Fig. 5 (c). Fringes of higher amplitude are present compared to those observed for Fig. 3 (c). The emergence of these fringes is a direct result of the minimization strategy, which does not aim at optimizing the latent (or unseen) function $\gamma(\xi)$, but rather optimizes the GP-DRT model parameters with respect to the given experimental evidence $Z_{im}^{exp}(f)$.
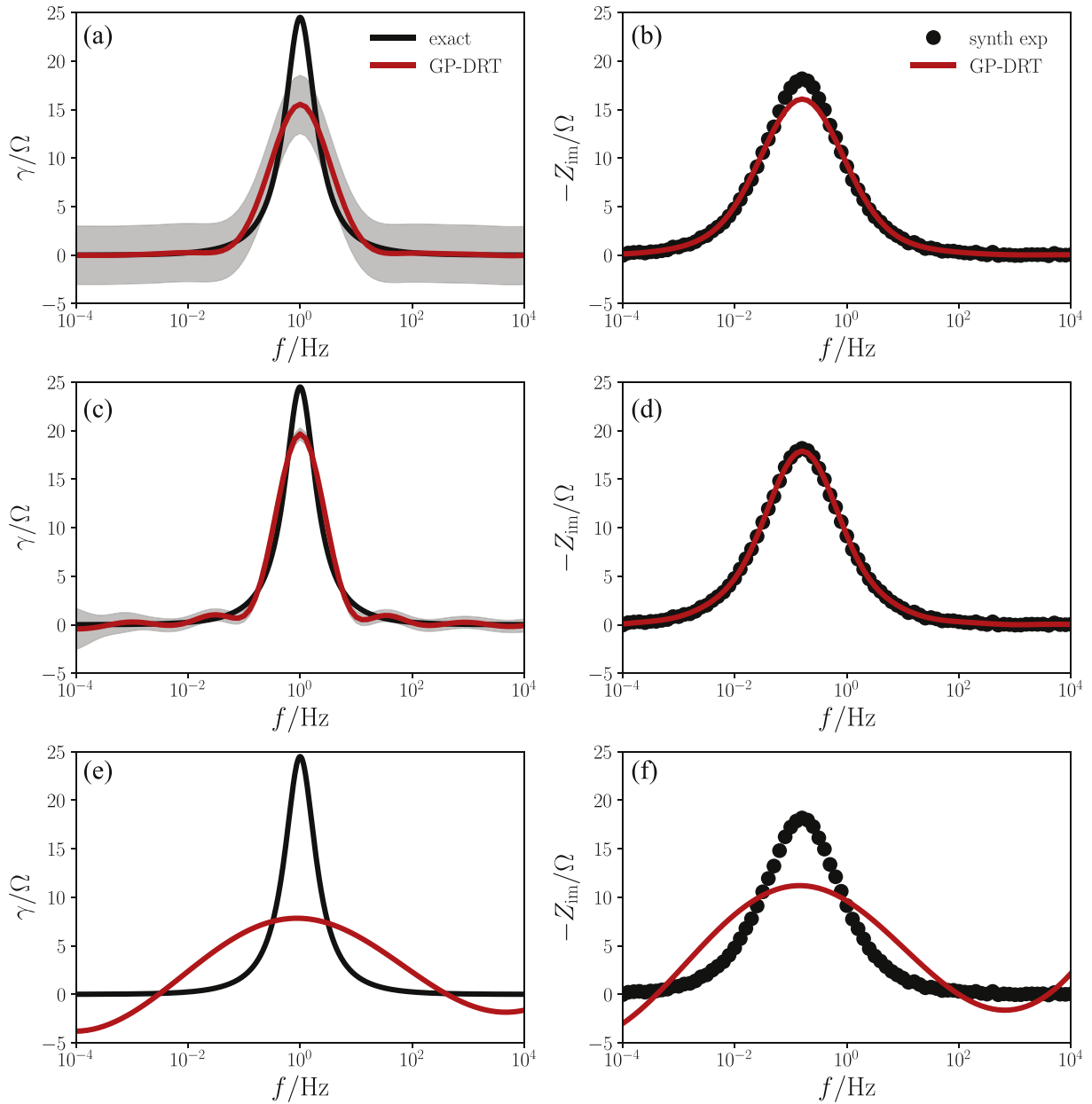
Fig. 3. Recovered DRT, γ, (left panels) and imaginary part of the impedance, Z_{im}, (right panels) for different kernel length scales: (a) and (b) $\ell = 10^{-2}$; (c) and (d) $\ell = 1$(c); and (e) and (f) $\ell = 10$. $\sigma_n = \sigma_n^{exp} = 0.1 \ \Omega^{1/2}$ was used for all plots.

3.1.4. Influence of experimental errors

The above discussion has shown that by using the imaginary part of the EIS data, one is able to recover the latent function, $\gamma(\xi)$. Since we have used only one computational experiment, we now wish to see if the qualitative conclusions drawn above still hold for more synthetic experiments and for larger experimental noise, σ_n^{exp}. To this end, 1000 synthetic experiments were generated using (16) for each $\sigma_n^{exp}/\Omega^{1/2} = 0.1, 0.2, \ldots, 1.0$. After generating each synthetic experiment, the optimal $\boldsymbol{\theta}$ by minimizing the NMLL function $L(\boldsymbol{\theta})$ was computed. Fig. 6 presents a box plot of the optimal $\boldsymbol{\theta}$'s over 10,000 stochastic experiments. The box extends from the 25% and 75% quartiles with the notch being the median. As seen in Fig. 6 (a), minimizing the NMLL leads to an accurate recovery of σ_n^{exp} by σ_n (the actual "experimental" values are plotted as the dashed line). Unsurprisingly, as we increase σ_n^{exp}, the

uncertainty on σ_n increases as evidenced by the larger box. The increased uncertainty of σ_n also holds for other two parameters ℓ and σ_f.

Fig. 7 explicitly reports the synthetic impedance $Z_{im}^{exp}(f)$, the inverted $\gamma(\xi)$, and the fitted $Z_{im}^{DRT}(f)$ for two synthetic experiments with $\sigma_n^{exp} = 1$ (panels (a), (c), and (e)) and $\sigma_n^{exp} = 3$ (panels (d), (d), and (f)). The optimal hyperparameters for these two experiments are also reported in Table 2 as case 2a and 2b, respectively. As σ_n^{exp} increases from 0.1 (Fig. 2) to 1 and 3, the impedance is far noisier, leading to larger uncertainties (gray regions) relative to $\gamma(\xi)$ and $Z_{im}^{DRT}(f)$. We must note two significant results: 1) in spite of the significant noise, the GP-DRT is still able to recover the correct mean impedance; and 2) the enlarged experimental uncertainty σ_n^{exp} is encoded directly in the model, which can quantitatively assess it by selecting (via the minimization of $L(\boldsymbol{\theta})$) the
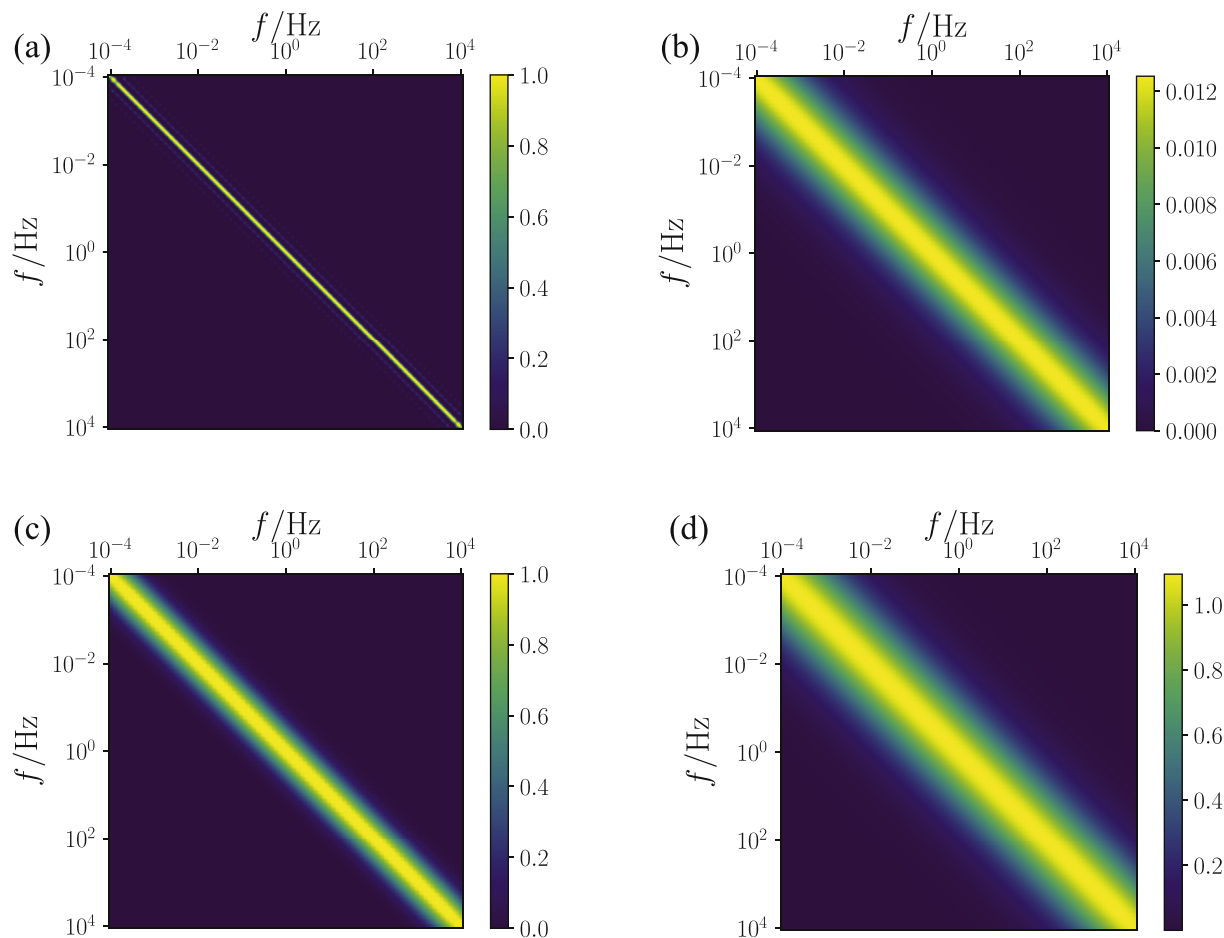
Fig. 4. Values of the entries of the, (a) and (b), **K** and, (b) and (d), $\mathscr{L}^2\mathbf{K}$ matrices. (a) and (b) correspond to $\ell = 10^{-2}$, while (c) and (d) to $\ell = 1$. The row and column numbers have been substituted by the corresponding frequencies.

Table 2
Optimal hyperparameters obtained by minimizing the NMLL function $L(\boldsymbol{\theta})$.

| Case	Description		σ_n	σ_f	ℓ	σ_L	Figure
1	Hyperparameter Optimization		8.44×10^{-2}	5.44	0.89		5 (c), 5 (d)
2a	Increased Experimental Errors	$\sigma_n^{\exp} = 1.0\,\Omega^{1/2}$	0.83	5.41	1.25		7 (c), 7 (e)
2b		$\sigma_n^{\exp} = 3.0\,\Omega^{1/2}$	2.45	5.33	1.40		7 (d), 7 (f)
3a	Truncated Data	at 10^{-3} Hz	0.10	5.80	0.94		8 (c), 8 (e)
3b		at 10^{-2} Hz	0.11	6.03	1.02		8 (d), 8 (f)
4a	Overlapping Timescales ($\tau_1 = 0.1$ s)	$\tau_2 = 10$ s	8.24×10^{-2}	7.81	0.86		9 (c), 9 (e)
4b		$\tau_2 = 1$ s	8.30×10^{-2}	8.17	0.83		9 (d), 9 (f)
5	Inductance Added		0.42	5.64	1.22	5.07×10^{-4}	10
6	SOFC Experiment		3.89×10^{-4}	3.85×10^{-3}	1.30	5.35×10^{-7}	11
7	LIB Experiment		1.37×10^{-4}	5.09×10^{-3}	0.37	6.37×10^{-7}	12

corresponding hyperparameter σ_n.

3.1.5. Truncated data and prediction

We now test if truncating the data at a certain frequency can still allow us to estimate $\gamma(\xi)$ and $Z_{\text{im}}^{\text{DRT}}(f)$ reasonably well. The same synthetic impedance data reported in Fig. 2 is used but it is truncated at 10^{-3} Hz, see Fig. 8 (a). The GP-DRT can be used to predict the $\gamma(\xi)$ beyond the experimental range (for $f < 10^{-3}$ Hz) as shown in Fig. 8 (c). While the predicted mean does not deviate significantly from the exact values, the standard deviation is particularly large, suggesting significant uncertainties. These uncertainties start before (at $f \approx 10^{-2}$ Hz) the enforced cut-off (at $f = 10^{-3}$ Hz) and

broaden significantly when approaching it. In contrast, the recovered $Z_{\text{im}}^{\text{DRT}}(f)$ appears to be compliant with the synthetic experiment only for $f \geq 10^{-3}$ Hz, see Fig. 8 (e). At lower frequencies, consistently with intuition, uncertainties increase and result in a widening of the credibility band.

It should be stressed again that the predicted values, both the hidden $\gamma(\xi)$ and the prediction $Z_{\text{im}}^{\text{DRT}}(f)$, are less reliable outside the measurement region. The same issues also emerge for EIS data truncated at 10^{-2} Hz. It is worth noting that, unsurprisingly, the optimal values of $\boldsymbol{\theta}$, which are reported in Table 2 as case 3a and 3b, are different from the ones used in case 1 in Table 2. Cutting off the impedance at low frequencies results in additional oscillations of
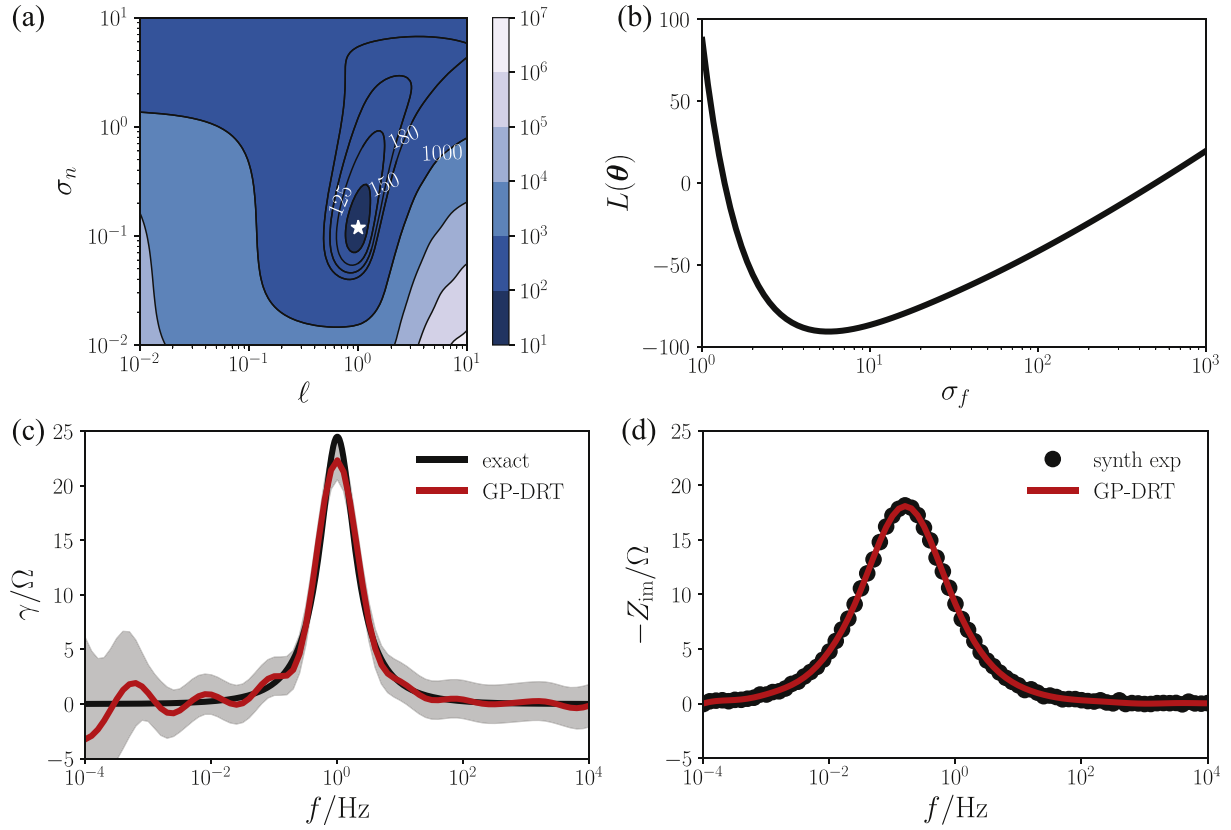
Fig. 5. (a) $L(\boldsymbol{\theta})$ as a function of ℓ and σ_n with $\sigma_f = 1$; (b) $L(\boldsymbol{\theta})$ versus σ_f with ℓ and σ_n at the values at the star symbol in panel (a). The recovered (c) DRT, γ, and (d) imaginary part of the impedance, Z_{im}.
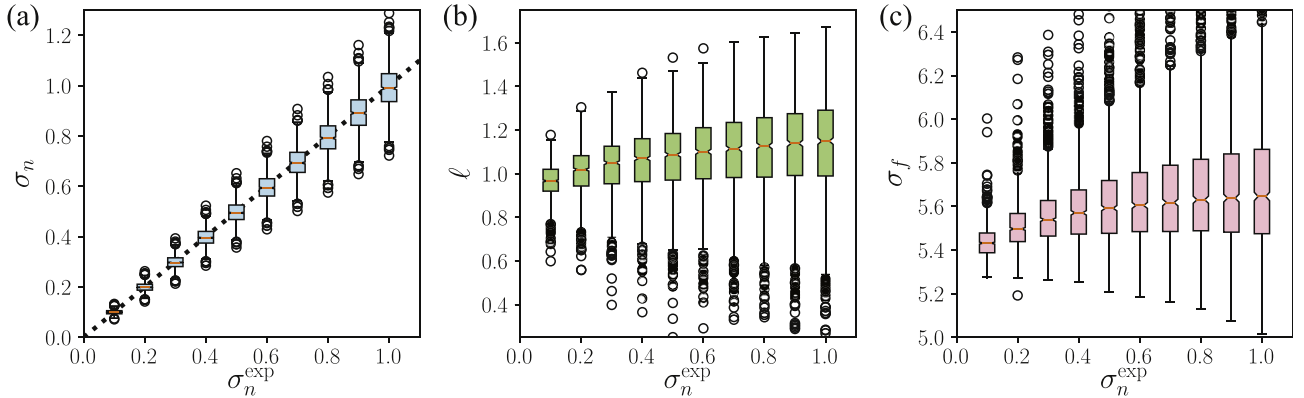
Fig. 6. Box plot of the optimal hyperparameters (a) σ_n, (b) σ_f, and (c) ℓ obtained by minimizing $L(\boldsymbol{\theta})$ over 10,000 stochastic experiments, 1000 for each σ_n^{exp} shown.

the DRT at high frequencies, see Fig. 8 (c) and (d) for $f > 10$ Hz. However, such fringes were not obviously present in untruncated data as illustrated in Fig. 5 (c). The larger the cutoff the more strongly the high frequency region is affected. This underpins the nature of the functional $\mathscr{L}_{\text{im}}(\cdot)$ that being a convolution leads to significant correlations in frequency space, as is apparent from (13b). Again, this result is consistent with the discussion in Section 3.1.2 regarding $\mathbf{K}$ and $\mathscr{L}^2\mathbf{K}$.

3.1.6. Overlapping frequencies

We will further test if the GP-DRT model can recover over-lapping features by summing two ZARCs, which have the following impedance response [49,57,73].

$$Z^{\text{exact}}(f) = 2R_\infty + \frac{1}{\frac{1}{R_{\text{ct}}} + C_1(i2\pi f)^\phi} + \frac{1}{\frac{1}{R_{\text{ct}}} + C_2(i2\pi f)^\phi} \quad (51)$$

with $C_1 = \frac{\tau_1^\phi}{R_{\text{ct}}}$, $C_2 = \frac{\tau_2^\phi}{R_{\text{ct}}}$ and specific parameters reported in Table 1. To generate the synthetic data shown in left-hand panels of Fig. 9, σ_n^{exp}
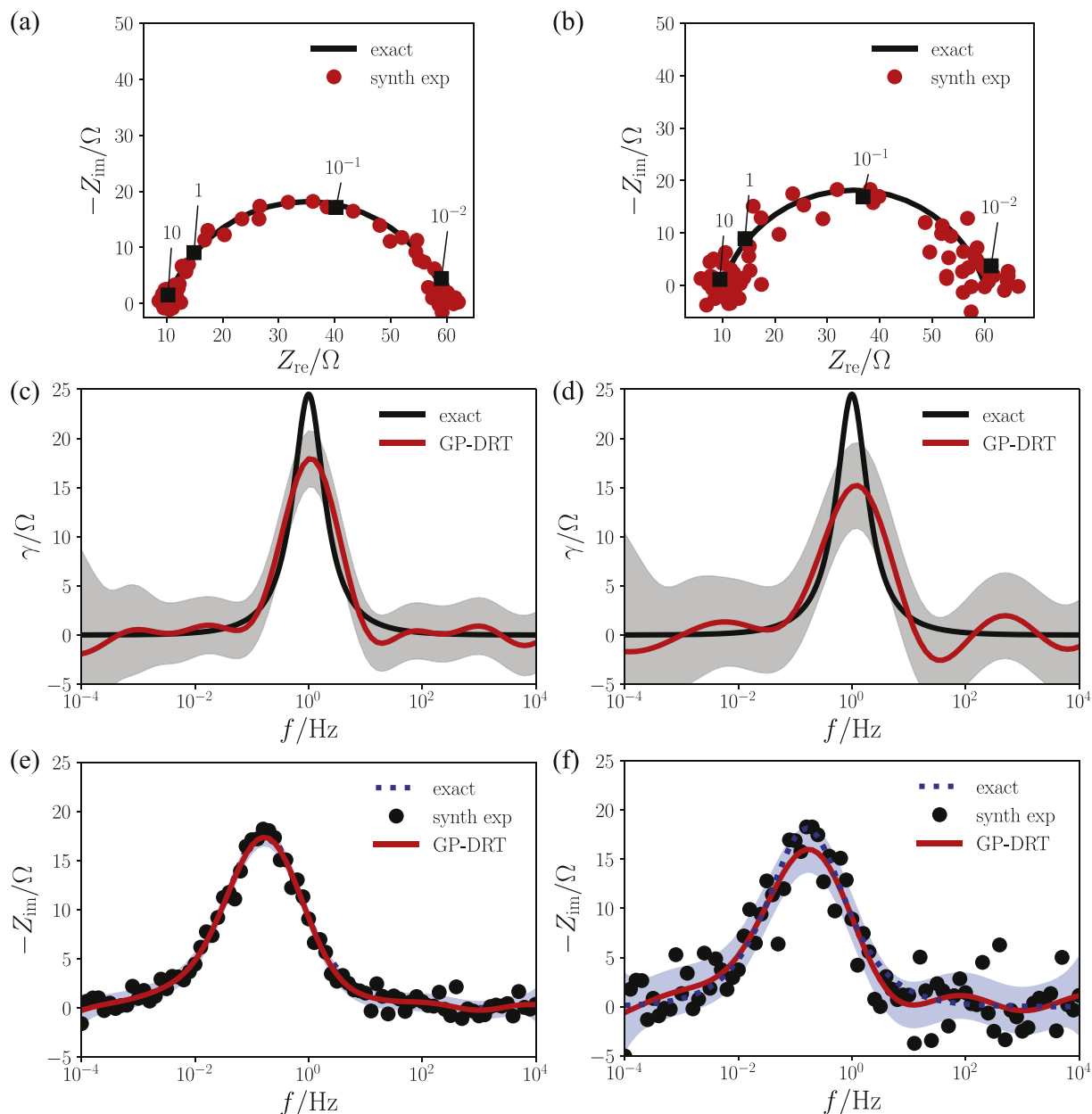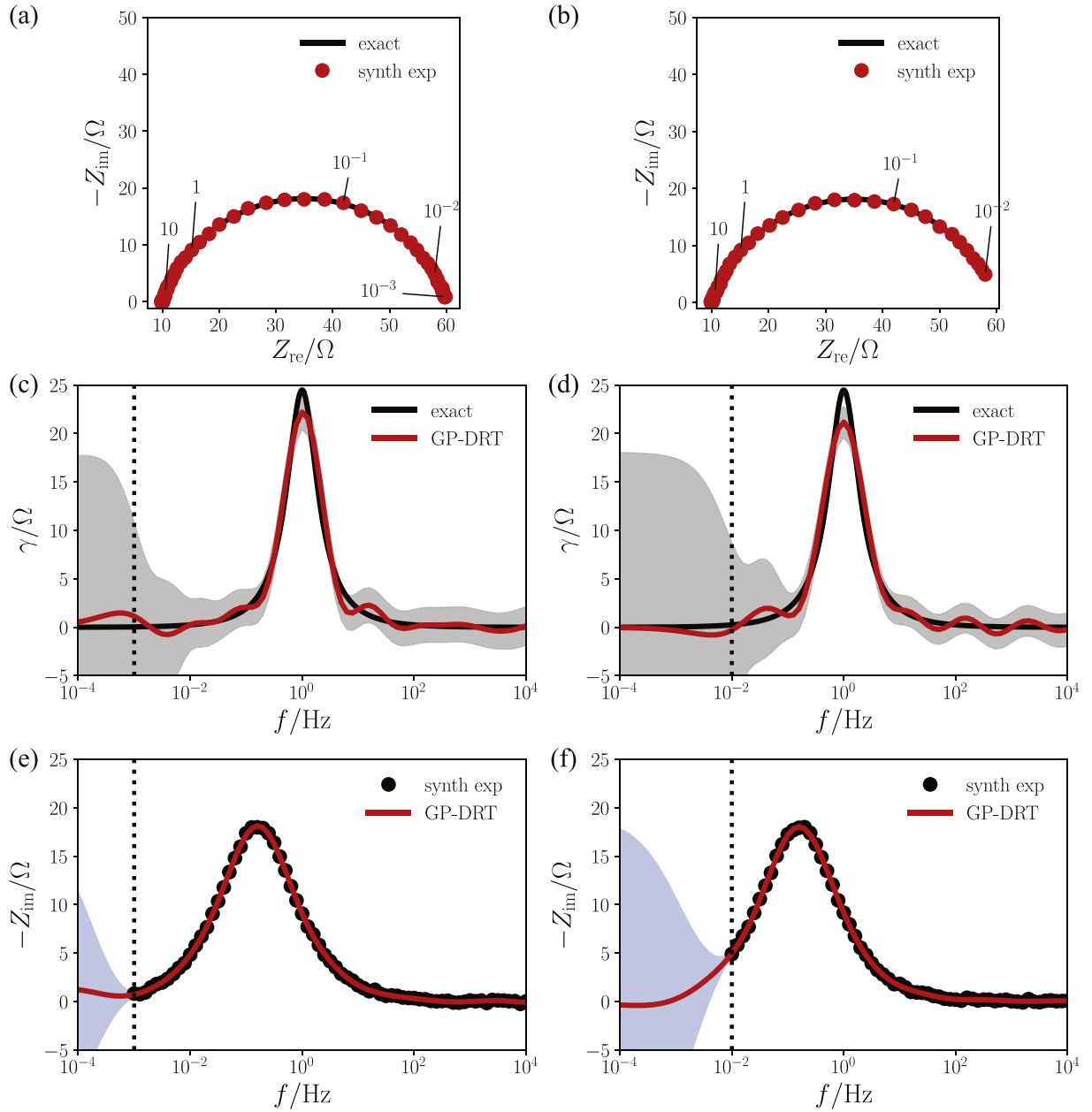
Fig. 7. Nyquist plot of synthetic experimental impedance with (a) $\sigma_n^{\mathrm{exp}} = 1.0 \ \Omega^{1/2}$ and (b) $\sigma_n^{\mathrm{exp}} = 3.0 \ \Omega^{1/2}$. The recovered $\gamma(\xi)$, (c) and (d), and $Z_{\mathrm{im}}(f)$, (e) and (f), are also shown. (c) and (e) correspond to $\sigma_n^{\mathrm{exp}} = 1.0 \ \Omega^{1/2}$, (panel a). (d) and (f) correspond to $\sigma_n^{\mathrm{exp}} = 3.0 \ \Omega^{1/2}$ (panel b).

is set to $0.1 \ \Omega^{1/2}$.

We first study separated timescales with $\tau_1 = 0.1$ s and $\tau_2 = 10$ s. The Nyquist plot reported in Fig. 9 (a) clearly shows two semicircles. The DRT obtained by (50) also depicts two well separated main peaks corresponding to above two different timescales, see Fig. 9 (c). By minimizing the NMLL function $L(\theta)$, the optimal hyparameters are obtained as listed in Table 2 and the recovered $\gamma(\xi)$ is also plotted in Fig. 9 (c). We find that the GP-DRT well fits the two main peaks of $\gamma(\xi)$ and estimates the mean of $\gamma(\xi)$ at higher frequencies for $f > 10^{-2}$ Hz. The uncertainties become higher at lower frequencies, which is also visible for a single ZARC model, see Fig. 5 (c).

To further test the capability of the GP-DRT model to recover overlapping DRT features, we reduce τ_2 by an order of magnitude

and keep τ_1 constant ($\tau_1 = 0.1$ s and $\tau_2 = 1.0$ s). As shown in Fig. 9 (b), the Nyquist plot appears visually as a single depressed semicircle. Further, the two peaks of the exact $\gamma(\xi)$ are much closer to each other, see Fig. 9 (d). The GP-DRT model with the hyperparameters given in Table 2 (case 4a and 4b) obtained by minimizing $L(\theta)$ can still capture the key features of the DRT and match the exact $\gamma(\xi)$ well. However, similar to the $\tau_2 = 10$ s case of Fig. 9 (c), oscillations with high variance appear at low frequencies. The recovered imaginary impedance $Z_{\mathrm{im}}^{\mathrm{DRT}}(f)$ for both cases are shown in Fig. 9 (e) and (f), which appear to adhere remarkably well to the exact value. While many more simulations will be needed in the future, these results suggest that the GP-DRT model can recover the exact DRT and the impedance even if there are overlapping features.

Fig. 8. Nyquist plot of synthetic experimental impedance data truncated at (a) 10^{-3} Hz and (b) 10^{-2} Hz; both plots have $\sigma_n^{\mathrm{exp}} = 0.1 \, \Omega^{1/2}$. The predicted DRT, γ, (c) and (d), and imaginary part of the impedance, Z_{im}, (e) and (f), are also shown.

3.1.7. Inductance

We then use the theory of Section 2.4 to obtain the DRT of the ZARC model (49) with an added inductance L_0. This corresponds to the following exact impedance:

$$Z^{\mathrm{exact}}(f) = i2\pi f L_0 + R_\infty + \cfrac{1}{\cfrac{1}{R_{\mathrm{ct}}} + C(i2\pi f)^\phi} \qquad (52)$$

In Fig. 10 (a) we report the $Z^{\mathrm{exp}}(f)$ for $\sigma_n^{\mathrm{exp}} = 0.1 \, \Omega^{1/2}$. 10,000 synthetic experiments (1000 experiments for each σ_n^{exp}) were carried out in the same spirit as the ones conducted in Section 3.1.4. The optimal hyperparameters σ_n and σ_L listed in Table 2 (case 5) can be used to estimate $\bar{L}_0$, see equation (44). The results of these simulations are reported as a boxplot in Fig. 10 (b). The average $\bar{L}_0$

consistently matches the exact value and its confidence region broadens as the noise increases, highlighting the ability of the GP-DRT to handle inductive features. The recovered DRT and impedance shown in Fig. 10 (c) and Fig. 10 (d), respectively, match well with the exact noise-free values.

3.2. Real experiments

3.2.1. SOFC impedance

We analyzed the EIS data obtained by testing a symmetrical cell with a $Ba_{0.95}La_{0.05}Fe_{0.95}P_{0.05}O_{3-\delta}$ electrode and 15% Samarium-doped ceria as the electrolyte with an active area of approximately $1cm^2$ [76]. The symmetrical cell's EIS spectrum shown in Fig. 11 (a), was measured at 700 °C in synthetic air ($p_{O_2} = 0.21$ atm)
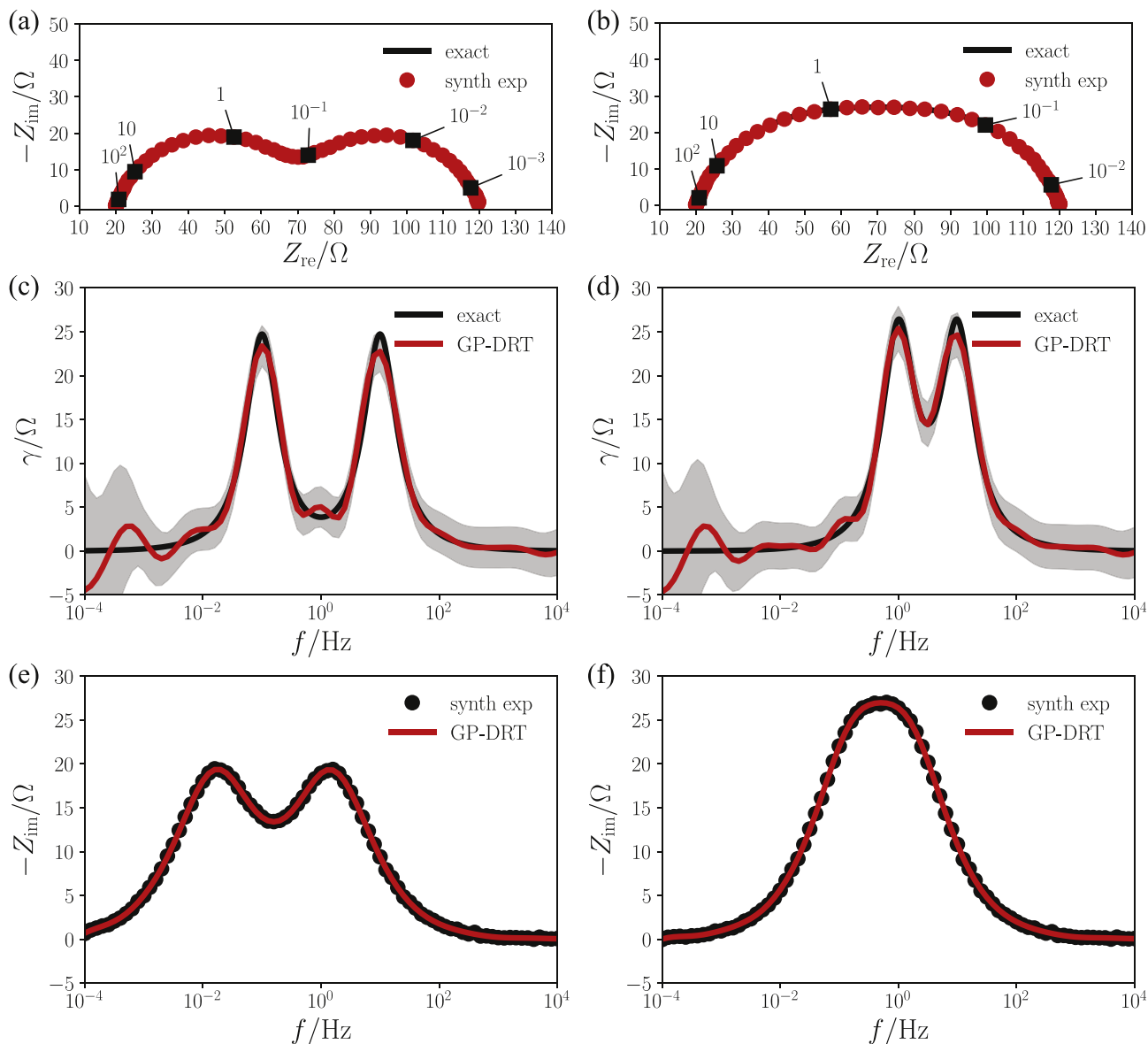
Fig. 9. Nyquist plot of the exact impedance (solid line) and synthetic experimental data (red dots) of two ZARCs with (a) $\tau_1 = 0.1$ s and $\tau_2 = 10$ s, and (b) $\tau_1 = 0.1$ s and $\tau_2 = 1.0$ s; both plots have $\sigma_n^{exp} = 0.1\ \Omega^{1/2}$. The recovered DRT, γ, (c) and (d), and imaginary part of the impedance, Z_{im}, (e) and (f) are also illustrated. (For interpretation of the references to colour in this figure legend, the reader is referred to the Web version of this article.)

over frequencies from 0.1 Hz to 2.47×10^4 Hz with 15 points per decade (ppd). The experimental data was first modeled as a single ZARC circuit, whose parameters are reported in Table 3. The Nyquist plot of the EIS generated by the chosen ECM is also shown in Fig. 11 (a). Using the ZARC model, $\gamma^{ref}(\xi)$ can be calculated using (50), see Fig. 11 (b). Following the same procedure used in Section 3.1.7, we minimize the NMLL, $L(\theta)$, to obtain the optimal hyperparameters used to recover the latent $\gamma(\xi)$ shown in Fig. 11 (b). It is noted that the GP-DRT matches well to $\gamma^{ref}(\xi)$'s main peak, which is located at $f \approx 10^4$ Hz. The $\gamma(\xi)$'s credibility is generally high but decreases away from the peak. In addition, the GP-DRT estimates $\bar{L}_0$ as 5.31×10^{-7} F, which is much close to the value fitted by ECM as listed in Table 3. We also conducted Bayesian RR [49] to compare the recovered $\gamma(\xi)$ against that obtained by GP-DRT. As illustrated in Fig. 11 (c), the RR deconvolution matches the $\gamma^{ref}(\xi)$ well and

displays a credibility higher than that of the GP-DRT. Lastly, Fig. 11 (d) shows the reconstructed imaginary parts of the EIS data by GP-DRT and RR. The two deconvolutions overlap and fit the $Z_{im}^{exp}(f)$ well. We must stress that, while the $Z_{im}(f)$ obtained using the GP-DRT is a GP with a narrow credibility band, its Bayesian RR counterpart is simply a function obtained by mapping of the maximum a posteriori prediction (the black line of Fig. 11 (c)) to the impedance.

3.2.2. Commercial LIB spectra

We used the GP-DRT model to analyze a previously reported EIS spectrum of a commercial lithium-ion battery (LIB) [57]. A commercial LIB (LiCoO$_2$-Ansmann 18650) was tested at 25% state of charge at room temperature. The EIS, which is reported in Fig. 12 (a), was collected from 5 mHz to 600 Hz. We chose this spectrum because it provides a challenging test for the GP-DRT model [66,77]. We first fitted the measured EIS to an ECM composed of 3 ZARCs:
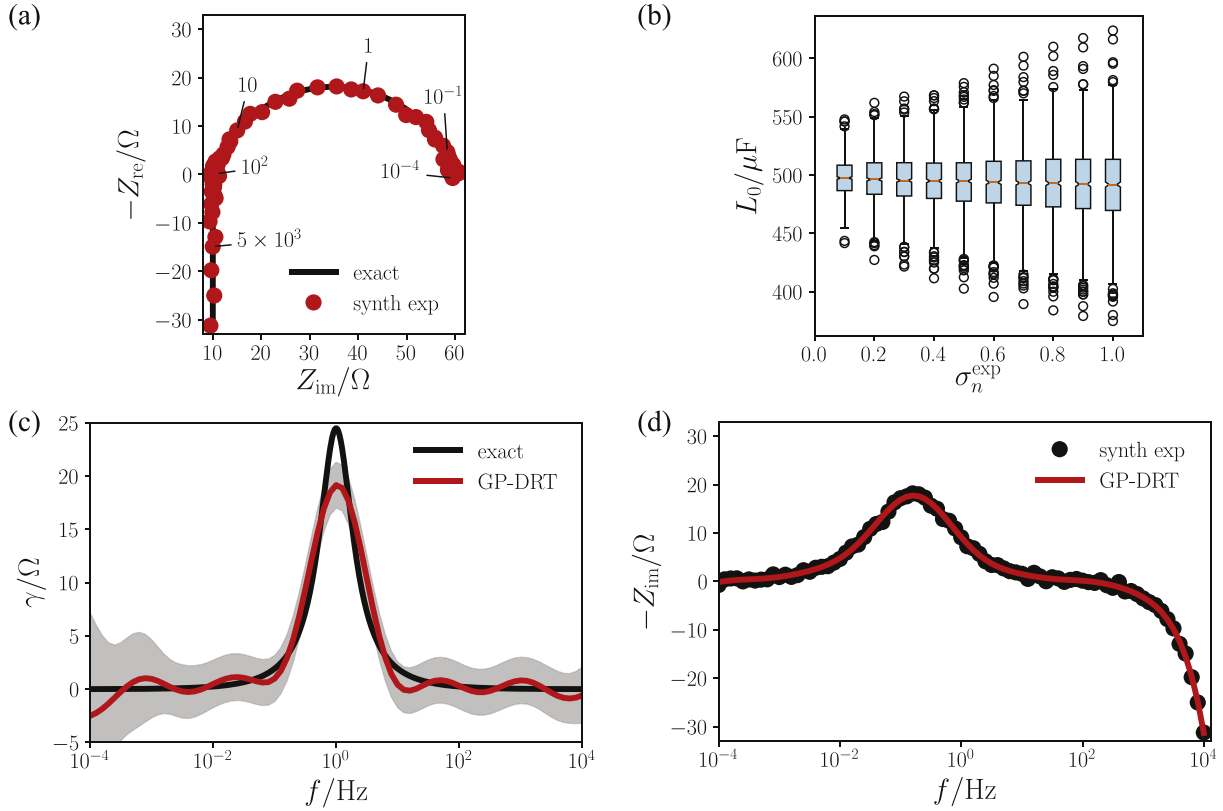
Fig. 10. (a) Nyquist plot of a single ZARC element plus an inductance ($\sigma_n^{\text{exp}} = 0.5 \ \Omega^{1/2}$). (b) Box plot of estimated $\overline{L}_0$ as a function of σ_n^{exp}. (c) Recovered DRT, γ, and (d) imaginary part of the impedance, Z_{im}.

$$Z_{\text{ECM}}(f) = i2\pi f L_0 + R_\infty + \cfrac{1}{\cfrac{1}{R_{\text{ct},1}} + C_1(i2\pi f)^{\phi_1}} + \cfrac{1}{\cfrac{1}{R_{\text{ct},2}} + C_2(i2\pi f)^{\phi_2}}$$

$$+ \cfrac{1}{\cfrac{1}{R_{\text{ct},3}} + C_3(i2\pi f)^{\phi_3}}$$

(53)

with the regressed parameters listed in Table 4. The DRT obtained by (50) is the $\gamma^{\text{ref}}(\xi)$ plotted in Fig. 12 (b) and (c) as a reference. As illustrated in Fig. 12 (b), the recovered $\gamma(\xi)$ by the GP-DRT model captures the $\gamma^{\text{ref}}(\xi)$'s main peaks and values. However, the mean value of the $\gamma(\xi)$ has stronger oscillations and a broader credibility region. The inductance $\overline{L}_0$ estimated by the GP-DRT is 5.20×10^{-7} F, a value matching the one obtained by the ECM fitting, see Table 4. Following our earlier publications [49,73], we also deconvolved the LIB spectrum using Bayesian RR to estimate the $\gamma(\xi)$, see Fig. 12 (c). It is noted that, unlike the GP-DRT framework, the Bayesian RR method has difficulty in matching well to the shape and the position of the main peaks of $\gamma^{\text{ref}}(\xi)$.

The recovered imaginary part of the impedance $Z_{\text{im}}^{\text{DRT}}(f)$ is shown in Fig. 12 (d) together with the imaginary experimental impedance $Z_{\text{im}}^{\text{exp}}(f)$. The GP-DRT approach matches the experimental data with a high credibility. In contrast, Bayesian RR shows clear discrepancy at low and high frequencies.

4. Perspective and future work

We have shown that the DRT can be interpreted as a GP. In

essence, GPs generalize Gaussian RVs and the GP-DRT extends the Bayesian DRT methods previously developed by our group [49,57,73]. In the GP-DRT, we first define the latent (or unseen) function $\gamma(\xi)$, which we identify as the DRT, to be a GP. We recall that $\xi = \log f = -\log \tau$ and that $\gamma(\xi)$ is indicated interchangeably as $\gamma(\log \tau)$, or $\gamma(\log f)$, and a similar notational abuse is used for $Z_{\text{im}}^{\text{DRT}}(f)$ and $Z_{\text{im}}^{\text{DRT}}(\xi)$. Then, we apply a linear functional to $\gamma(\xi)$ to obtain $Z_{\text{im}}^{\text{DRT}}(\xi)$, the imaginary part of the impedance. In doing that, we show that $\gamma(\xi)$ and $Z_{\text{im}}^{\text{DRT}}(\xi)$ are two correlated GPs. The GP-DRT consistently manages to identify the hyperparameters without sacrificing computational tractability. The GP-DRT can be used to solve two major challenges: 1) the inverse problem of determining the DRT given the impedance data; and 2) the prediction of the impedance together with its credibility. It is important to note that one of the most striking features of GP-DRT is that it overcomes the limitations of all approaches used to date for the analysis of the DRT. This is because it allows us to select the hyperparameters rationally by maximizing the experimental evidence.

Despite being highly effective, the GP-DRT has a few shortcomings, which are not addressed in this report. First, as it is currently formulated, the GP-DRT does not allow using the real part of the data. Second, we have not enforced any constraint on the DRT, for example, there are no constraints set for $\gamma(\xi)$ with $\gamma(\xi) \geq 0$. Third, we implement the current GP-DRT only with a squared exponential kernel. Hereon, we will suggests methodologies that can be used to tackle these two issues.

4.1. Including the real part of the data

Equation (35) highlights one major limitation of the current
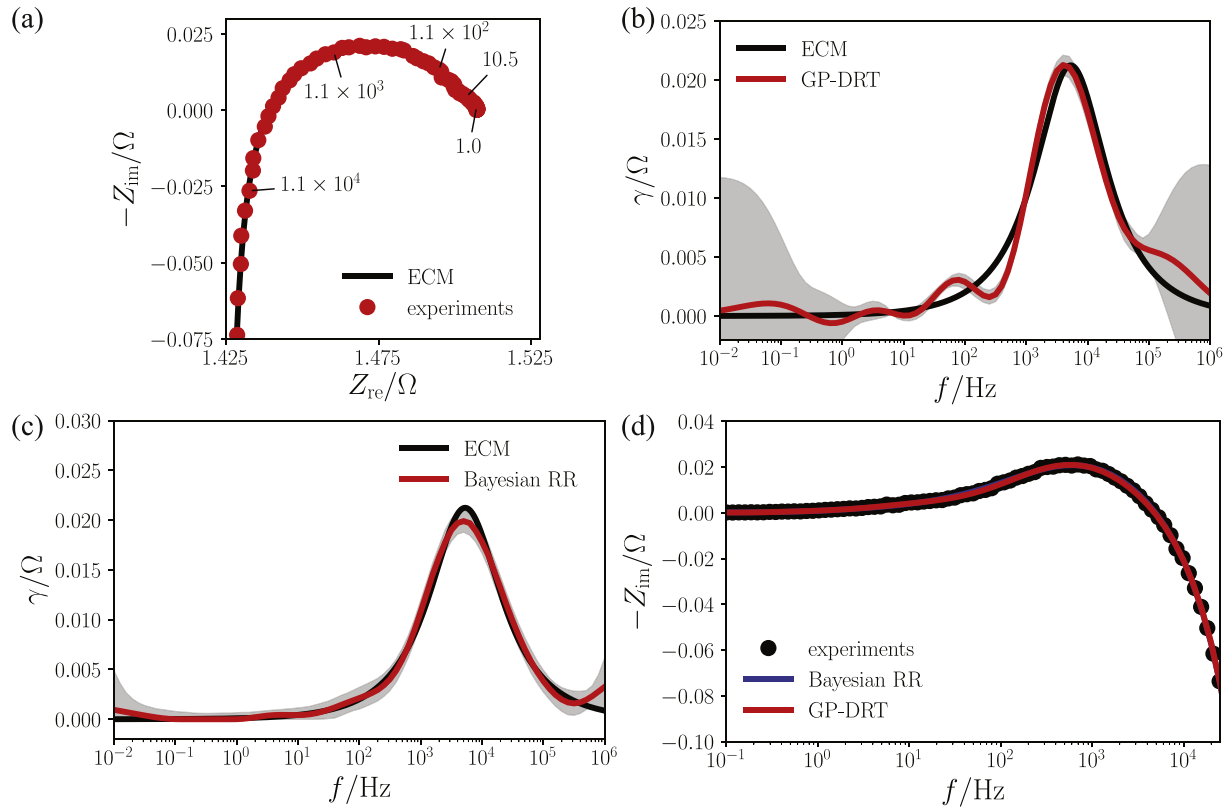
Fig. 11. (a) Nyquist plot of the impedance of the experimental SOFC data (red dots) and fitted ECM (solid line). Recovered DRT, γ, by (b) the GP-DRT method and (c) Bayesian RR, where in both panels the DRT of the reference ECM is also shown. (d) The imaginary part of the impedance, Z_{im}, obtained by the GP-DRT (red) and Bayesian RR (blue) and comparison with the experimental EIS. (For interpretation of the references to colour in this figure legend, the reader is referred to the Web version of this article.)

Table 3
ECM parameters obtained by fitting the EIS spectrum of the SOFC shown in Fig. 11.

Parameter	Numerical Value
R_∞	$1.42\ \Omega$
R_{ct}	$8.41 \times 10^{-2}\ \Omega$
τ_0	$1.88 \times 10^{-4}\ s$
ϕ	0.64
L_0	$5.20 \times 10^{-7}\ F$

formulation of the GP-DRT: using the real part of the impedance data leads to infinite entries in the covariance matrix. Such an inconsistency can be overcome if bounds of integration are changed in the functionals. For example, the following can be defined:

$$\mathscr{L}_\xi^{re}(\cdot) = \int_{\xi_{min}}^{\xi_{max}} \frac{1}{1 + (2\pi e^{\xi - \widehat{\xi}})^2}(\cdot)\,d\widehat{\xi} \tag{54a}$$

$$\mathscr{L}_\xi^{im}(\cdot) = -\int_{\xi_{min}}^{\xi_{max}} \frac{2\pi e^{\xi - \widehat{\xi}}}{1 + (2\pi e^{\xi - \widehat{\xi}})^2}(\cdot)\,d\widehat{\xi} \tag{54b}$$

4.2. Positivity constraint

As seen in the many examples above, the latent $\gamma(\xi)$ estimated using the GP-DRT model often oscillates away from the peak, especially at the rim of the frequency spectrum. Also, the GP-DRT

model repeatedly leads to estimated $\gamma(\xi)$'s that are not positive everywhere, where negative values of $\gamma(\xi)$ are unphysical. Such a limitation can be overcome by constraining the latent variable $\gamma(\xi)$ to be positive. Inspired by works on classification [67,78], this constraint can be implemented by modifying the joint posterior to include a probit likelihood prior that enforces $\gamma(\xi) \geq 0$ [79]. Algorithmically, this is done by approximating the corresponding probability density functions (PDFs) either with a Laplace approximation or an expectation propagation algorithm [80,81].

4.3. Choosing the kernel

In this work, we constrained the kernel, see Section 2.3.4, to be a single squared exponential with a length scale parameter ℓ. However, this is not the only choice; different kernels or combination of kernels could have been used [67]. In principle, instead of defining the kernels in advance, the structures of kernels could have been inferred from the data [82] for example by leveraging the Kramers-Kronig relationships [50] and their connection to the Hilbert transform [83]. Also, the selection of kernel functions and parameter estimation can also be implemented by the combination of GPs and the approximate Bayesian computation algorithm [84].

5. Conclusions

In this work, we have developed the GP-DRT model. The GP-DRT is a novel theoretical framework based on GP that recovers the DRT from EIS data using analytical expressions without the need for choosing the model hyperparameters arbitrarily. The model assumes that the DRT, $\gamma(\xi)$, is a GP. Using the definition of DRT and its
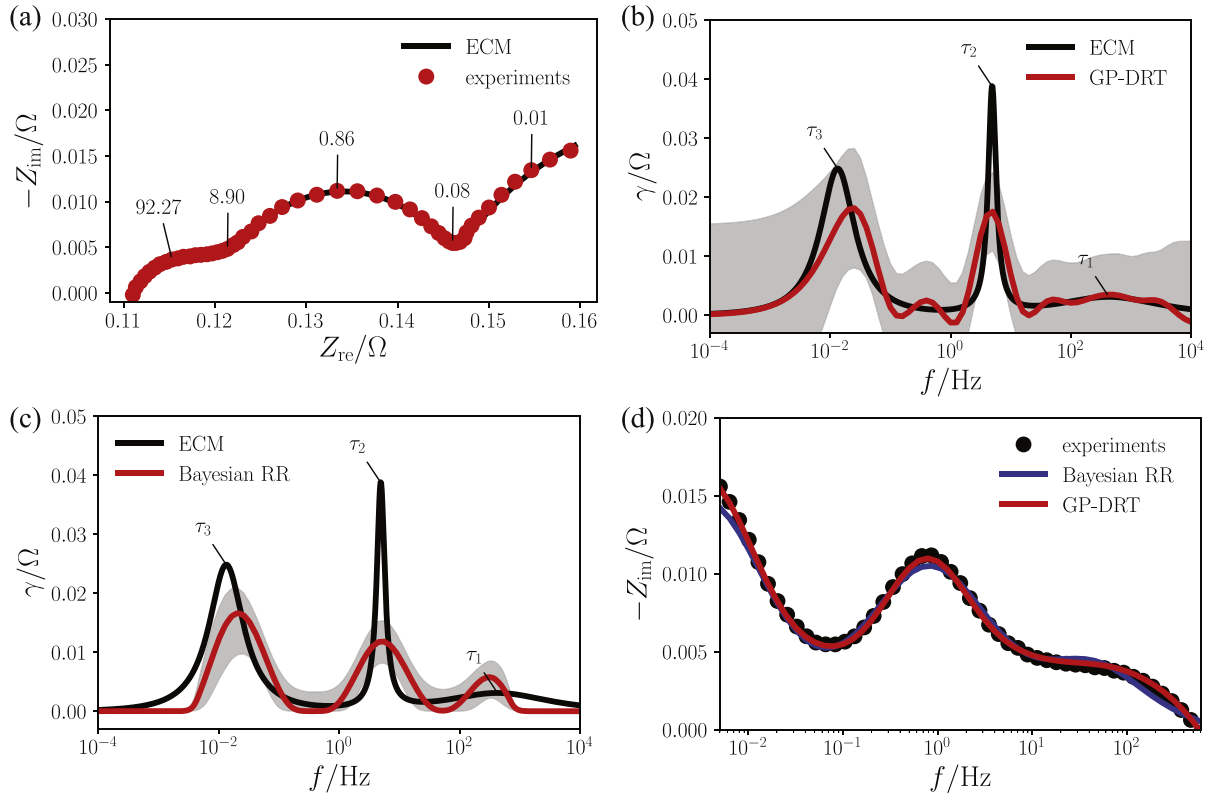
Fig. 12. (a) Nyquist plot of the EIS response of a commercial LIB (red dots) fitted using an ECM consisting of 3 ZARCs (solid line). Recovered DRT, γ, by (b) the GP-DRT method and (c) Bayesian RR. (d) The recovered imaginary part of the impedance, Z_{im}, by GP-DRT (red) and Bayesian RR (blue) compared with the experimental data. (For interpretation of the references to colour in this figure legend, the reader is referred to the Web version of this article.)

Table 4
ECM parameters obtained by fitting the EIS spectrum of the LIB shown in Fig. 12.

Parameter	Numerical Value
R_∞	0.11 Ω
$R_{ct,1}$	1.69×10^{-2} Ω
$R_{ct,2}$	2.12×10^{-2} Ω
$R_{ct,3}$	5.23×10^{-2} Ω
τ_1	2.34×10^{-3} s
τ_2	0.20 s
τ_3	75.30 s
ϕ_1	0.54
ϕ_2	0.94
ϕ_3	0.79
L_0	7.61×10^{-7} F

relationship to the impedance, it follows that the imaginary part of the impedance, $Z_{im}^{DRT}(f)$, is also a GP. Therefore, the PDFs of $\gamma(\xi)$ and $Z_{im}^{DRT}(f)$ can be obtained by conditioning with respect to the experimental data. While the performance of the GP-DRT model is strongly affected by its hyperparameters, they can be chosen rationally by maximizing the experimental evidence (*i.e.*, minimizing the NLLM $L(\boldsymbol{\theta})$). Both synthetic experiments and real experiments indicate that the GP-DRT framework is capable of recovering both the latent DRT and the impedance, even for measurements with a high noise level, overlapping timescales, or incomplete (spectrally truncated) data. In reference to the latter issues, the GP-DRT can predict the impedance values and their uncertainty at unmeasured frequencies. Moreover, the GP-DRT model can include the inductances without deteriorating its performance.

We also observe that the GP-DRT model performs well when "real" experiments are analyzed. The method is particularly well suited to fit the imaginary part of the impedance data. This feature is attributed to the strategy used to optimize the hyperparameters. These hyperparameters are obtained by maximizing the likelihood of the experimental data.

In summary, the GP-DRT model proposed in this article provides a completely new approach to DRT analysis. Not only can the credibility of the obtained results be assessed, but also the model hyperparameters can be chosen rationally. This approach will certainly stimulate further work and improvement in this area.

Code availability

Code for tutorial examples is available at https://github.com/ciuccislab/GP-DRT.

Declaration of interest statement

The authors declare that there is no competing interest.

Author Contributions Section

F.C. conceived the idea and derived the theoretical part of the main text. J.L. and F.C. carried out the calculation, wrote the paper, and edited the manuscript together.

Acknowledgements

List of abbreviations and symbols

$\gamma(\xi)$	Distribution of relaxation times, also written as $\gamma(\log f)$ or $\gamma(\log \tau)$
$g(\tau)$	Distribution function
$\gamma^{\mathrm{ref}}(\xi)$	Reference solution of DRT
$\mathbf{Z}^{\exp}$	Vector of experimental impedance
$Z^{\exp}(f)$	Experimental impedance, also written as $Z^{\exp}(\xi)$
$Z^{\mathrm{DRT}}(f)$	Impedance by DRT, also written as $Z^{\mathrm{DRT}}(\xi)$
$\mathscr{L}_\xi(\cdot)$	Linear functional
μ	Mean function of GP
$\mathbf{K}$	Covariance matrix of GP
$\mathbf{I}$	Indentity matrix
Σ	Covariance matrix of GP with respect to observations
$k(\xi,\xi')$	Kernel function
ε	Random error
σ_n	Standard deviation of experimental impedance noise
σ_L	Standard deviation of inductance noise
σ_f	Hyperparameter of kernel function
ℓ	Hyperparameter of length scale in kernel function
$L(\boldsymbol{\theta})$	Negative marginal log-likelihood
$\nabla L(\boldsymbol{\theta})$	Gradient of negative marginal log-likelihood
$\boldsymbol{\theta}$	Hyperparameter vector
τ	Relaxation time
τ_0	Characteristic relaxation time
ϕ	Parameter of constant phase element
f	Frequency
ξ	log-frequency
λ	Regularizing parameter
L_0	Inductance
R_∞	Ohmic resistance
R_{ct}	Charge transfer resistance
CPE	Constant phase element
DRT	Distribution of relaxation times
ECM	Equivalent circuit model
ECS	Electrochemical system
EIS	Electrochemical impedance spectroscopy
GP	Gaussian process
NMLL	Negative marginal log-likelihood
PDF	Probability density function
RR	Ridge regression
RV	Random variable

Appendix A. Multivariate Gaussian Random Variables

We recall that a multivariate Gaussian RV $\mathbf{z}$ with mean $\boldsymbol{\mu}$ and a positive definite covariance matrix $\Sigma > 0$ is defined as $\mathbf{z} \sim \mathscr{N}(\boldsymbol{\mu}, \Sigma)$ and its probability distribution function is

$$p(\mathbf{z}) = \mathscr{N}(\mathbf{z}|\boldsymbol{\mu}, \Sigma) = \left((2\pi)^N \det(\Sigma)\right)^{-\frac{1}{2}}$$
$$\exp\left(-\frac{1}{2}(\mathbf{z}-\boldsymbol{\mu})^\top \Sigma^{-1}(\mathbf{z}-\boldsymbol{\mu})\right) \quad (55)$$

For notational convenience, we can partition the Gaussian RV as follows:

$$\mathbf{z} = \begin{pmatrix} \mathbf{x} \\ \mathbf{y} \end{pmatrix} \quad (56)$$

where the corresponding means and covariances are

$$\boldsymbol{\mu} = \begin{pmatrix} \boldsymbol{\mu}_x \\ \boldsymbol{\mu}_y \end{pmatrix} \quad (57a)$$

$$\Sigma = \begin{pmatrix} \Sigma_{xx} & \Sigma_{xy} \\ \Sigma_{xy}^\top & \Sigma_{yy} \end{pmatrix} \quad (57b)$$

Below, we apply marginalization and conditioning and write the PDF of $\mathbf{x}$ and of $\mathbf{x}|\mathbf{y}$, respectively.

A.1. Marginalization

Using (56) and (57), we can obtain the PDF of $\mathbf{x}$ by integrating $\mathbf{y}$ out as

$$p(\mathbf{x}) = \int p(\mathbf{z}|\boldsymbol{\mu}, \Sigma)\, d\mathbf{y} = \mathscr{N}(\mathbf{x}|\boldsymbol{\mu}_x, \Sigma_{xx}) \quad (58)$$

or equivalently we can write

$$\mathbf{x} \sim \mathscr{N}(\boldsymbol{\mu}_x, \Sigma_{xx}) \quad (59)$$

A.2. Conditioning

The probability of $\mathbf{x}$ known $\mathbf{y}$ is defined as follows:

$$p(\mathbf{x}|\mathbf{y}) = \frac{p(\mathbf{x}, \mathbf{y})}{p(\mathbf{y})} = \mathscr{N}(\mathbf{x}|\boldsymbol{\mu}_{x|y}, \Sigma_{x|y}) \quad (60)$$

where

$$\boldsymbol{\mu}_{x|y} = \boldsymbol{\mu}_x + \Sigma_{xy}\Sigma_{yy}^{-1}(\mathbf{y} - \boldsymbol{\mu}_y) \quad (61a)$$

$$\Sigma_{x|y} = \Sigma_{xx} - \Sigma_{xy}\Sigma_{yy}^{-1}\Sigma_{xy}^\top \quad (61b)$$

or equivalently

$$\mathbf{x}|\mathbf{y} \sim \mathscr{N}(\boldsymbol{\mu}_{x|y}, \Sigma_{x|y}) \quad (62)$$

Appendix B. Matrices Used in the GP-DRT: Derivations and Properties

B.1. $\mathscr{L}_{im}\mathbf{K}$ and $\mathscr{L}_{im}^\sharp\mathbf{K}$

We consider the kernel to be radial, i.e., $k(\xi,\xi') = k(|\xi - \xi'|)$, and recall (15) and (18b)

$$\mathscr{L}_{\xi'}^{\mathrm{im}}(k(\xi,\xi')) = -\int_{-\infty}^{\infty} \frac{2\pi e^{\xi'-\widehat{\xi}}}{1 + (2\pi e^{\xi'-\widehat{\xi}})^2} k(\xi,\widehat{\xi})\, d\widehat{\xi} \quad (63)$$

Specifically, the (18b) can be written explicitly as

$$\mathscr{L}_{\mathrm{im}}\mathbf{K}(\xi_n,\xi_m)=\left|\mathscr{L}_{\xi'}^{\mathrm{im}}(k(\xi,\xi'))\right||_{\xi_n,\xi_m}=$$

$$-\int_{-\infty}^{\infty}\frac{2\pi e^{\xi_m-\widehat{\xi}}}{1+(2\pi e^{\xi_m-\widehat{\xi}})^2}k(\xi_n,\widehat{\xi})\,\mathrm{d}\widehat{\xi} \tag{64}$$

If we define $\chi=\widehat{\xi}-\xi_n$, then we can also write that

$$\mathscr{L}_{\mathrm{im}}\mathbf{K}(\xi_n,\xi_m)=-\int_{-\infty}^{\infty}\frac{2\pi e^{\Delta\xi_{mn}-\chi}}{1+(2\pi e^{\Delta\xi_{mn}-\chi})^2}k(\chi)\,\mathrm{d}\chi \tag{65}$$

where $\Delta\xi_{mn}=\xi_m-\xi_n$. We note that, if the frequencies are logarithmically equispaced (the number of points per decade is set), then $\mathscr{L}_{\mathrm{im}}\mathbf{K}$ is a Toeplitz matrix, a matrix whose descending diagonals are constant. This reduces significantly the computation time as, instead of computing the full N^2 integrals, only $2N-1$ are needed. We also note that

$$\mathscr{L}_{\xi}^{\mathrm{im}}(k(\xi,\xi'))=-\int_{-\infty}^{\infty}\frac{2\pi e^{\xi-\widehat{\xi}}}{1+(2\pi e^{\xi-\widehat{\xi}})^2}k(\widehat{\xi},\xi')\,\mathrm{d}\widehat{\xi} \tag{66}$$

which gives that

$$\mathscr{L}_{\mathrm{im}}^{\sharp}\mathbf{K}(\xi_n,\xi_m)=\left|\mathscr{L}_{\xi}^{\mathrm{im}}(k(\xi,\xi'))\right||_{\xi_n,\xi_m}=$$

$$-\int_{-\infty}^{\infty}\frac{2\pi e^{\xi_n-\widehat{\xi}}}{1+(2\pi e^{\xi_n-\widehat{\xi}})^2}k(\widehat{\xi},\xi_m)\,\mathrm{d}\widehat{\xi} \tag{67}$$

Defining $\chi=\widehat{\xi}-\xi_m$ we can write that

$$\mathscr{L}_{\mathrm{im}}^{\sharp}\mathbf{K}(\xi_n,\xi_m)=-\int_{-\infty}^{\infty}\frac{2\pi e^{\Delta\xi_{nm}-\chi}}{1+(2\pi e^{\Delta\xi_{nm}-\chi})^2}k(\chi)\,\mathrm{d}\chi \tag{68}$$

It follows that by comparing (65) and (68) that

$$\mathscr{L}_{\mathrm{im}}^{\sharp}\mathbf{K}(\xi_n,\xi_m)=\mathscr{L}_{\mathrm{im}}\mathbf{K}(\xi_m,\xi_n) \tag{69}$$

and that

$$\mathscr{L}_{\mathrm{im}}^{\sharp}\mathbf{K}=\mathscr{L}_{\mathrm{im}}\mathbf{K}^{\top} \tag{70}$$

B.2. $\mathscr{L}_{im}^2\mathbf{K}$

Interestingly, we can transform (18d) from a double integral into a single integral. We first recall (18d)

$$\mathscr{L}_{\mathrm{im}}^2\mathbf{K}(\xi_n,\xi_m)=$$

$$\int_{-\infty}^{\infty}\int_{-\infty}^{\infty}\frac{2\pi e^{\xi_n-\xi'}}{1+(2\pi e^{\xi_n-\xi'})^2}\frac{2\pi e^{\xi_m-\xi''}}{1+(2\pi e^{\xi_m-\xi''})^2}k(\xi',\xi'')\,\mathrm{d}\xi'\,\mathrm{d}\xi'' \tag{71}$$

We perform a change of variables by setting $\chi=\xi'-\xi''$ and $\chi'=\xi'+\xi''$. We note that the Jacobian of this transformation is

$$\frac{\partial(\chi,\chi')}{\partial(\xi',\xi'')}=\begin{pmatrix}1&-1\\1&1\end{pmatrix} \tag{72}$$

therefore

$$\mathrm{d}\chi\,\mathrm{d}\chi'=\det\left(\frac{\partial(\chi,\chi')}{\partial(\xi',\xi'')}\right)\mathrm{d}\xi'\,\mathrm{d}\xi''=2\,\mathrm{d}\xi'\,\mathrm{d}\xi'' \tag{73}$$

The (18d) can be rewritten as

$$\mathscr{L}_{\mathrm{im}}^2\mathbf{K}(\xi_n,\xi_m)=$$

$$\frac{1}{2}\int_{-\infty}^{\infty}\left(\int_{-\infty}^{\infty}\frac{2\pi e^{\xi_n-\frac{\chi+\chi'}{2}}}{1+\left(2\pi e^{\xi_n-\frac{\chi+\chi'}{2}}\right)^2}\frac{2\pi e^{\xi_m-\frac{\chi'-\chi}{2}}}{1+\left(2\pi e^{\xi_m-\frac{\chi'-\chi}{2}}\right)^2}\mathrm{d}\chi'\right)k(\chi)\,\mathrm{d}\chi \tag{74}$$

The inner integral is

$$\int_{-\infty}^{\infty}\frac{(2\pi)^2 e^{\xi_n+\xi_m-\chi'}}{\left(1+(2\pi)^2 e^{2\xi_n-(\chi+\chi')}\right)\left(1+(2\pi)^2 e^{2\xi_m-(\chi'-\chi)}\right)}\,\mathrm{d}\chi' \tag{75}$$

$$=(\chi+\Delta\xi_{mn})\mathrm{csch}(\chi+\Delta\xi_{mn})$$

where $\mathrm{csch}(z)=\frac{2}{e^z-e^{-z}}$. This procedure allows us to simplify (18d) as:

$$\mathscr{L}_{\mathrm{im}}^2\mathbf{K}(\xi_n,\xi_m)=\frac{1}{2}\int_{-\infty}^{\infty}(\chi+\Delta\xi_{mn})\mathrm{csch}(\chi+\Delta\xi_{mn})k(\chi)\,\mathrm{d}\chi \tag{76}$$

Incidentally, we note that $\mathscr{L}_{\mathrm{im}}^2\mathbf{K}$ is symmetrical, *i.e.*, $\mathscr{L}_{\mathrm{im}}^2\mathbf{K}=\mathscr{L}_{\mathrm{im}}^2\mathbf{K}^{\top}$ or equivalently $(\mathscr{L}_{\mathrm{im}}^2\mathbf{K})_{nm}=\mathscr{L}_{\mathrm{im}}^2\mathbf{K}(\xi_n,\xi_m)=\mathscr{L}_{\mathrm{im}}^2\mathbf{K}(\xi_m,\xi_n)=(\mathscr{L}_{\mathrm{im}}^2\mathbf{K})_{mn}$, because swapping ξ_n and ξ_m in (18d), does not change the integrand. Furthermore, if the frequencies are equispaced logarithmically, then $\mathscr{L}_{\mathrm{im}}^2\mathbf{K}$ is a Toeplitz matrix.

B.3. $\mathscr{L}_{re}^2\mathbf{K}$

We note that the following holds:

$$\mathscr{L}_{\xi'}^{\mathrm{re}}\left(\mathscr{L}_{\xi}^{\mathrm{re}}(k(\xi,\xi'))\right)|_{\xi_n,\xi_m}$$

$$=\int_{-\infty}^{\infty}\int_{-\infty}^{\infty}\frac{1}{1+(2\pi e^{\xi_n-\xi'})^2}\frac{1}{1+(2\pi e^{\xi_m-\xi''})^2}k(\xi',\xi'')\,\mathrm{d}\xi'\,\mathrm{d}\xi''$$

$$=\infty \tag{77}$$

as the integrand does not tend to zero if. $\xi',\xi''\to\infty$

Appendix C. Gradient of marginal log-likelihhod (MLL)

In order to compute the minimum of $L(\boldsymbol{\theta})$, we use gradients and note that [67].

$$\frac{\partial}{\partial\theta_j}L(\boldsymbol{\theta})=-\frac{1}{2}\mathbf{Z}_{\mathrm{im}}^{\mathrm{exp}\top}\mathbf{A}(\boldsymbol{\theta})^{-1}\left(\frac{\partial}{\partial\theta_j}\mathbf{A}(\boldsymbol{\theta})\right)\mathbf{A}(\boldsymbol{\theta})^{-1}\mathbf{Z}_{\mathrm{im}}^{\mathrm{exp}}++\frac{1}{2}\mathrm{tr}(\mathbf{A}(\boldsymbol{\theta})^{-1}\left(\frac{\partial}{\partial\theta_j}\mathbf{A}(\boldsymbol{\theta})\right)) \tag{78}$$

where if $\boldsymbol{\theta} = (\sigma_n, \sigma_f, \ell)^\top$, then

$$\mathbf{A}(\boldsymbol{\theta}) = \mathscr{L}_{\text{im}}^2 \mathbf{K}\left(\sigma_f, \ell\right) + \sigma_n^2 \mathbf{I} \tag{79}$$

or if $\boldsymbol{\theta} = (\sigma_n, \sigma_f, \ell, \sigma_L)^\top$, then

$$\mathbf{A}(\boldsymbol{\theta}) = \mathscr{L}_{\text{im}}^2 \mathbf{K}\left(\sigma_f, \ell\right) + \sigma_n^2 \mathbf{I} + \sigma_L^2 \mathbf{h}\mathbf{h}^\top \tag{80}$$

References

[1] A.J. Bard, L.R. Faulkner, J. Leddy, C.G. Zoski, Electrochemical Methods: Fundamentals and Applications, vol. 2, Wiley, New York, 1980.

[2] E. Barsoukov, J.R. Macdonald, Impedance Spectroscopy: Theory, Experiment, and Applications, John Wiley & Sons, 2018.

[3] A. Frumkin, Advances in Electrochemistry and Electrochemical Engineering, vol. 3, Interscience Pub., New York, 1963, p. 307.

[4] A. Lasia, Electrochemical Impedance Spectroscopy and its Applications, Springer US, Boston, MA, 2002, pp. 143−248.

[5] M.E. Orazem, B. Tribollet, Electrochemical Impedance Spectroscopy, vol. 48, John Wiley & Sons, 2011.

[6] W. Lai, S.M. Haile, Impedance spectroscopy as a tool for chemical and electrochemical analysis of mixed conductors: a case study of ceria, J. Am. Ceram. Soc. 88 (11) (2005) 2979−2997.

[7] F. Ciucci, Modeling electrochemical impedance spectroscopy, Curr. Opinion Electrochem. 13 (2019) 132−139.

[8] M.J. Jørgensen, M. Mogensen, Impedance of solid oxide fuel cell LSM/YSZ composite cathodes, J. Electrochem. Soc. 148 (5) (2001) A433−A442.

[9] V. Sonn, A. Leonide, E. Ivers-Tiffée, Combined deconvolution and cnls fitting approach applied on the impedance response of technical Ni/8YSZ cermet electrodes, J. Electrochem. Soc. 155 (7) (2008) B675−B679.

[10] A. Leonide, V. Sonn, A. Weber, E. Ivers-Tiffée, Evaluation and modeling of the cell resistance in anode-supported solid oxide fuel cells, J. Electrochem. Soc. 155 (1) (2008) B36−B41.

[11] S. Dierickx, J. Joos, A. Weber, E. Ivers-Tiffée, Advanced impedance modelling of Ni/8YSZ cermet anodes, Electrochim. Acta 265 (2018) 736−750.

[12] S. Dierickx, T. Mundloch, A. Weber, E. Ivers-Tiffée, Advanced impedance model for double-layered solid oxide fuel cell cermet anodes, J. Power Sources 415 (2019) 69−82.

[13] E.-C. Shin, J. Ma, P.-A. Ahn, H.-H. Seo, D.T. Nguyen, J.S. Lee, Deconvolution of four transmission-line-model impedances in ni-ysz/ysz/lsm solid oxide cells and mechanistic insights, Electrochim. Acta 188 (2016) 240−253.

[14] R. Mohammadi, M. Søgaard, T. Ramos, M. Ghassemi, M.B. Mogensen, Electrochemical impedance modeling of a solid oxide fuel cell anode, Fuel Cells 14 (4) (2014) 645−659.

[15] J.P. Schmidt, T. Chrobak, M. Ender, J. Illig, D. Klotz, E. Ivers-Tiffée, Studies on LiFePO$_4$as cathode material using impedance spectroscopy, J. Power Sources 196 (12) (2011) 5342−5348.

[16] W. Waag, S. Käbitz, D.U. Sauer, Experimental investigation of the lithium-ion battery impedance characteristic at various conditions and aging states and its influence on the application, Appl. Energy 102 (2013) 885−897.

[17] C. Chen, J. Liu, K. Amine, Symmetric cell approach and impedance spectroscopy of high power lithium-ion batteries, J. Power Sources 96 (2) (2001) 321−328.

[18] B. Scrosati, F. Croce, L. Persi, Impedance spectroscopy study of peo-based nanocomposite polymer electrolytes, J. Electrochem. Soc. 147 (5) (2000) 1718−1721.

[19] S. Zhang, K. Xu, T. Jow, Eis study on the formation of solid electrolyte interface in li-ion battery, Electrochim. Acta 51 (8−9) (2006) 1636−1640.

[20] J. Illig, M. Ender, A. Weber, E. Ivers-Tiffée, Modeling graphite anodes with serial and transmission line models, J. Power Sources 282 (2015) 335−347.

[21] P. Braun, C. Uhlmann, M. Weiss, A. Weber, E. Ivers-Tiffée, Assessment of all-solid-state lithium-ion batteries, J. Power Sources 393 (2018) 119−127.

[22] F. Fabregat-Santiago, J. Bisquert, G. Garcia-Belmonte, G. Boschloo, A. Hagfeldt, Influence of electrolyte in transport and recombination in dye-sensitized solar cells studied by impedance spectroscopy, Sol. Energy Mater. Sol. Cells 87 (1−4) (2005) 117−131.

[23] Q. Wang, J.E. Moser, M. Grätzel, Electrochemical impedance spectroscopic analysis of dye-sensitized solar cells, J. Phys. Chem. B 109 (31) (2005) 14945−14953.

[24] R. Kötz, M. Hahn, R. Gallay, Temperature behavior and impedance fundamentals of supercapacitors, J. Power Sources 154 (2) (2006) 550−555.

[25] U.G. Kyle, I. Bosaeus, A.D. De Lorenzo, P. Deurenberg, M. Elia, J.M. Gómez, B.L. Heitmann, L. Kent-Smith, J.-C. Melchior, M. Pirlich, et al., Bioelectrical impedance analysis—part i: review of principles and methods, Clin. Nutr. 23 (5) (2004) 1226−1243.

[26] E. Katz, I. Willner, Probing biomolecular interactions at conductive and semiconductive surfaces by impedance spectroscopy: routes to impedimetric immunosensors, dna-sensors, and enzyme biosensors, Electroanalysis: An Int.

[27] M.D. Van Loan, P. Withers, J. Matthie, P.L. Mayclin, Use of bioimpedance spectroscopy to determine extracellular fluid, intracellular fluid, total body water, and fat-free mass, in: Human Body Composition, Springer, 1993, pp. 67−70.

[28] W. Franks, I. Schenker, P. Schmutz, A. Hierlemann, Impedance characterization and modeling of electrodes for biomedical applications, IEEE (Inst. Electr. Electron. Eng.) Trans. Biomed. Eng. 52 (7) (2005) 1295−1302.

[29] R. Go, R. Bashir, A. Sarikaya, M. Ladisch, J. Sturgis, J. Robinson, T. Geng, A. Bhunia, H. Apple, S. Wereley, et al., Microfluidic biochip for impedance spectroscopy of biological species, Biomed. Microdevices 3 (3) (2001) 201−209.

[30] J. Song, M.Z. Bazant, Electrochemical impedance imaging via the distribution of diffusion times, Phys. Rev. Lett. 120 (11) (2018) 116001.

[31] J.R. Macdonald, Comparison of parametric and nonparametric methods for the analysis and inversion of immittance data: critique of earlier work, J. Comput. Phys. 157 (1) (2000) 280−301.

[32] D.D. Macdonald, Reflections on the history of electrochemical impedance spectroscopy, Electrochim. Acta 51 (8−9) (2006) 1376−1388.

[33] J. Fleig, Impedance spectroscopy on solids: the limits of serial equivalent circuit models, J. Electroceram. 13 (1−3) (2004) 637−644.

[34] A. Nenning, A. Opitz, T. Huber, J. Fleig, A novel approach for analyzing electrochemical properties of mixed conducting solid oxide fuel cell anode materials by impedance spectroscopy, Phys. Chem. Chem. Phys. 16 (40) (2014) 22321−22336.

[35] J. Maier, Physical Chemistry of Ionic Materials: Ions and Electrons in Solids, John Wiley & Sons, 2004.

[36] C. Chen, D. Chen, W.C. Chueh, F. Ciucci, Modeling the impedance response of mixed-conducting thin film electrodes, Phys. Chem. Chem. Phys. 16 (23) (2014) 11573−11583.

[37] F. Ciucci, W.C. Chueh, D.G. Goodwin, S.M. Haile, Surface reaction and transport in mixed conductors with electrochemically-active surfaces: a 2-d numerical study of ceria, Phys. Chem. Chem. Phys. 13 (6) (2011) 2121−2135.

[38] J. Liu, F. Ciucci, Modeling the impedance spectra of mixed conducting thin films with exposed and embedded current collectors, Phys. Chem. Chem. Phys. 19 (38) (2017) 26310−26321.

[39] J. Jamnik, J. Maier, Generalised equivalent circuits for mass and charge transport: chemical capacitance and its implications, Phys. Chem. Chem. Phys. 3 (9) (2001) 1668−1678.

[40] J. Horno, A. Moya, C. González-Fernández, Simulation and interpretation of electrochemical impedances using the network method, J. Electroanal. Chem. 402 (1−2) (1996) 73−80.

[41] A. Moya, J. Horno, Application of the network simulation method to ionic transport in ion-exchange membranes including diffuse double-layer effects, J. Phys. Chem. B 103 (49) (1999) 10791−10799.

[42] J. Bisquert, Theory of the impedance of electron diffusion and recombination in a thin layer, J. Phys. Chem. B 106 (2) (2002) 325−333.

[43] M. Doyle, J.P. Meyers, J. Newman, Computer simulations of the impedance response of lithium rechargeable batteries, J. Electrochem. Soc. 147 (1) (2000) 99−110.

[44] J.P. Meyers, M. Doyle, R.M. Darling, J. Newman, The impedance response of a porous electrode composed of intercalation particles, J. Electrochem. Soc. 147 (8) (2000) 2930−2940.

[45] E. Ivers-Tiffee, A. Weber, Evaluation of electrochemical impedance spectra by the distribution of relaxation times, J. Ceram. Soc. Jpn. 125 (4) (2017) 193−201.

[46] K. Kobayashi, T.S. Suzuki, Distribution of relaxation time analysis for non-ideal immittance spectrum: discussion and progress, J. Phys. Soc. Jpn. 87 (9) (2018) 094002.

[47] Y. Zhang, Y. Chen, M. Li, M. Yan, M. Ni, C. Xia, A high-precision approach to reconstruct distribution of relaxation times from electrochemical impedance spectroscopy, J. Power Sources 308 (2016) 1−6.

[48] F. Ciucci, C. Chen, Analysis of electrochemical impedance spectroscopy data using the distribution of relaxation times: a bayesian and hierarchical bayesian approach, Electrochim. Acta 167 (2015) 439−454.

[49] T.H. Wan, M. Saccoccio, C. Chen, F. Ciucci, Influence of the discretization methods on the distribution of relaxation times deconvolution: implementing radial basis functions with drttools, Electrochim. Acta 184 (2015) 483−499.

[50] B.A. Boukamp, Fourier transform distribution function of relaxation times; application and limitations, Electrochim. Acta 154 (2015) 35−46.

[51] S.J. Cooper, A. Bertei, D.P. Finegan, N.P. Brandon, Simulated impedance of diffusion in porous media, Electrochim. Acta 251 (2017) 681−689.

[52] P.S. Sabet, D.U. Sauer, Separation of predominant processes in electrochemical impedance spectra of lithium-ion batteries with nickelmanganesecobalt cathodes, J. Power Sources 425 (2019) 121−129.

[53] D. Clematis, S. Presto, M.P. Carpanese, A. Barbucci, F. Deganello, L.F. Liotta, C. Aliotta, M. Viviani, Distribution of relaxation times and equivalent circuits analysis of Ba$_{0.5}$Sr$_{0.5}$Co$_{0.8}$Fe$_{0.2}$O$_{3-\delta}$, Catalysts 9 (5) (2019) 441.

[54] X. Zhou, J. Huang, Z. Pan, M. Ouyang, Impedance characterization of lithium-ion batteries aging under high-temperature cycling: importance of electrolyte-phase diffusion, J. Power Sources 426 (2019) 216−222.

[55] B.A. Boukamp, A. Rolle, Use of a distribution function of relaxation times (dfrt) in impedance analysis of sofc electrodes, Solid State Ion. 314 (2018) 103−111.

[56] B.A. Boukamp, A. Rolle, Analysis and application of distribution of relaxation times in solid state ionics, Solid State Ion. 302 (2017) 12−18.

[57] M. Saccoccio, T.H. Wan, C. Chen, F. Ciucci, Optimal regularization in distribution of relaxation times applied to electrochemical impedance spectroscopy: ridge and lasso regression methods-a theoretical and experimental study, Electrochim. Acta 147 (2014) 470−482.

[58] T. Hörlin, Deconvolution and maximum entropy in impedance spectroscopy of noninductive systems, Solid State Ion. 107 (3−4) (1998) 241−253.

[59] M. Eckert, L. Kölsch, S. Hohmann, Fractional algebraic identification of the distribution of relaxation times of battery cells, in: 2015 54th IEEE Conference on Decision and Control (CDC), IEEE, 2015, pp. 2101−2108.

[60] E. Tuncer, S. Gubanski, On dielectric data analysis. using the Monte Carlo method to obtain relaxation time distribution and comparing non-linear spectral function fits, IEEE Trans. Dielectr. Electr. Insul. 8 (3) (2001) 310−320.

[61] A. Tesler, D. Lewin, S. Baltianski, Y. Tsur, Analyzing results of impedance spectroscopy using novel evolutionary programming techniques, J. Electroceram. 24 (4) (2010) 245−260.

[62] S. Hershkovitz, S. Baltianski, Y. Tsur, Harnessing evolutionary programming for impedance spectroscopy analysis: a case study of mixed ionic-electronic conductors, Solid State Ion. 188 (1) (2011) 104−109.

[63] S. Hershkovitz, S. Tomer, S. Baltianski, Y. Tsur, Isgp: impedance spectroscopy analysis using evolutionary programming procedure, ECS Trans. 33 (40) (2011) 67−73.

[64] Y. Zhang, Y. Chen, M. Yan, F. Chen, Reconstruction of relaxation time distribution from linear electrochemical impedance spectroscopy, J. Power Sources 283 (2015) 464−477.

[65] X. Li, M. Ahmadi, L. Collins, S.V. Kalinin, Deconvolving distribution of relaxation times, resistances and inductance from electrochemical impedance spectroscopy via statistical model selection: exploiting structural-sparsity regularization and data-driven parameter tuning, Electrochim. Acta 313 (2019) 570−583.

[66] F. Ciucci, T. Carraro, W.C. Chueh, W. Lai, Reducing error and measurement time in impedance spectroscopy using model based optimal experimental design, Electrochim. Acta 56 (15) (2011) 5416−5434.

[67] C.K. Williams, C.E. Rasmussen, Gaussian Processes for Machine Learning, vol. 2, MIT Press Cambridge, MA, 2006.

[68] K.P. Murphy, Machine Learning: a Probabilistic Perspective, MIT press, 2012.

[69] S. Särkkä, Linear operators and stochastic partial differential equations in Gaussian process regression, in: Proceedings of the 21st International Conference on Artificial Neural Networks - Volume Part II, ICANN'11, Springer-Verlag, Berlin, Heidelberg, 2011, pp. 151−158.

[70] C.E. Rasmussen, Gaussian processes in machine learning, in: Summer School on Machine Learning, Springer, 2003, pp. 63−71.

[71] A. O'Hagan, Curve fitting and optimal design for prediction, J. R. Stat. Soc. Ser. B 40 (1) (1978) 1−24.

[72] A. Papoulis, S.U. Pillai, Probability, Random Variables, and Stochastic Processes, Tata McGraw-Hill Education, 2002.

[73] M.B. Effat, F. Ciucci, Bayesian and hierarchical bayesian based regularization for deconvolving the distribution of relaxation times from electrochemical impedance spectroscopy data, Electrochim. Acta 247 (2017) 1117−1129.

[74] S. Buller, M. Thele, E. Karden, R.W.D. Doncker, Impedance-based non-linear dynamic battery modeling for automotive applications, J. Power Sources, in: Proceedings of the International Conference on Lead-Acid Batteries, vol. 113, LABAT '02, 2003, pp. 422−430, 2.

[75] F. Dion, A. Lasia, The use of regularization methods in the deconvolution of underlying distributions in electrochemical processes, J. Electroanal. Chem. 475 (1) (1999) 28−37.

[76] J. Liu, J. Wang, A. Belotti, F. Ciucci, P-substituted $Ba_{0.95}La_{0.05}FeO_{3-\tau}$ as a cathode material for sofcs, ACS Appl. Energy Mater. 2 (8) (2019) 5472−5480.

[77] F. Ciucci, Revisiting parameter identification in electrochemical impedance spectroscopy: weighted least squares and optimal experimental design, Electrochim. Acta 87 (2013) 532−545.

[78] H. Nickisch, C.E. Rasmussen, Approximations for binary Gaussian process classification, J. Mach. Learn. Res. 9 (Oct) (2008) 2035−2078.

[79] J. Riihimäki, A. Vehtari, Gaussian processes with monotonicity information, in: Proceedings of the Thirteenth International Conference on Artificial Intelligence and Statistics, 2010, pp. 645−652.

[80] T.P. Minka, Expectation propagation for approximate bayesian inference, in: Proceedings of the Seventeenth Conference on Uncertainty in Artificial Intelligence, Morgan Kaufmann Publishers Inc., 2001, pp. 362−369.

[81] M. Kuss, C.E. Rasmussen, Assessing approximate inference for binary Gaussian process classification, J. Mach. Learn. Res. 6 (Oct) (2005) 1679−1704.

[82] D. Duvenaud, J. R. Lloyd, R. Grosse, J. B. Tenenbaum, Z. Ghahramani, Structure Discovery in Nonparametric Regression through Compositional Kernel Search, arXiv Preprint arXiv:1302.4922.

[83] L. Ambrogioni, E. Maris, Integral Transforms from Finite Data: an Application of Gaussian Process Regression to Fourier Analysis, arXiv Preprint arXiv:1704.02828.

[84] A.B. Abdessalem, N. Dervilis, D.J. Wagg, K. Worden, Automatic kernel selection for Gaussian processes regression with approximate bayesian computation and sequential Monte Carlo, Front. Built Environ. 3 (2017) 52.